

Saint-Petersburg National Research University of Information Technology,  
Mechanics and Optics  
Faculty of Laser and Light Engineering

Department of Nanophotonics and Metamaterials

Pavel Alekseevich Dmitriev

# Resonant Optical Properties of Crystalline Dielectric Nanoparticles, Fabricated by Laser Ablation-Based Methods

Master's Thesis

12.04.03 — Nanophotonics and Metamaterials

Admitted for defence.  
Head of the chair:  
D. Sc. P. A. Belov

Scientific supervisor:  
Dr. S. V. Makarov  
Dr. A. K. Samusev

Reviewer:

Saint-Petersburg  
2017

# Contents

<b>Introduction</b>	<b>4</b>
<b>1. Dielectric Nanophotonics</b>	<b>5</b>
1.1. Crystalline Silicon as the Material of Choice for Dielectric Nanophotonics . . . . .	5
1.2. Analytical Models . . . . .	5
1.2.1. Mie-Type Resonances of Dielectric Nanoparticles . . . . .	5
1.2.2. Raman Scattering from Crystalline Materials . . . . .	6
1.3. Numerical Models . . . . .	7
1.3.1. Discrete Dipole Approximation . . . . .	7
1.3.2. Finite Element Method . . . . .	7
1.3.3. Finite Difference Time Domain . . . . .	8
1.3.4. Finite Integration Technique . . . . .	8
1.4. Fabrication of Dielectric Nanoparticles . . . . .	8
1.4.1. Chemical Synthesis . . . . .	8
1.4.2. Thin-Film Dewetting . . . . .	9
1.4.3. Laser Ablation-Based Methods . . . . .	9
1.4.4. Lithographic Methods . . . . .	9
1.5. Experimental Characterization Methods . . . . .	10
1.5.1. Electron Microscopy . . . . .	10
1.5.1.1. Transmission Electron Microscopy . . . . .	10
1.5.1.2. Scanning Electron Microscopy . . . . .	10
1.5.2. Optical Characterization . . . . .	10
1.5.2.1. Elastic Scattering — Dark Field Microscopy . . . . .	11
1.5.2.2. Inelastic Scattering — Raman Scattering . . . . .	11
1.5.3. Scanning Probe Methods . . . . .	11
1.6. Goals . . . . .	11
<b>2. Methods</b>	<b>13</b>
2.1. Fabrication of Crystalline Silicon Nanoparticles by Femtosecond Laser Ablation .	13
2.1.1. Laser Transfer of Crystalline Dielectric Particles . . . . .	13
2.1.2. Laser Writing of Dielectric Particles . . . . .	14
2.2. Optical Measurements . . . . .	15
2.2.1. Polarization-Resolved Dark-field Spectroscopy of Single Nanoparticles .	15
2.2.2. Raman Spectroscopy of Single Nanoparticles . . . . .	15
2.3. Analytical Model of Raman Signal Enhancement by Mie resonances of Nanoparticles	16
2.3.1. Numerical Methods . . . . .	18
2.3.2. Discrete Dipole Approximation . . . . .	19

2.3.3. Finite Integration Technique . . . . .	20
<b>3. Experimental Results</b>	<b>21</b>
3.1. Fabrication of Crystalline Silicon Nanoparticles . . . . .	21
3.1.1. Laser Writing of Nanoparticles . . . . .	21
3.1.2. Laser Transfer of Nanoparticles . . . . .	22
3.2. Characterization of Resonant Optical Modes of the Nanoparticles . . . . .	23
3.3. Determining Size of Nanoparticle from Optical Resonance Positions . . . . .	24
3.4. Raman Scattering Enhancement from Single Nanoparticles . . . . .	25
<b>Results</b>	<b>28</b>
<b>Acknowledgements</b>	<b>29</b>
<b>A. Mie Scattering of Light</b>	<b>30</b>
A.1. Maxwell's Equations . . . . .	30
A.2. Scalar Solution . . . . .	31
A.3. Vector Solution . . . . .	32
A.4. Incident, Scattered and Internal Fields . . . . .	33
A.5. Mie Coefficients . . . . .	34
A.6. Cross Sections . . . . .	35
<b>B. Raman Scattering from Crystalline Materials</b>	<b>37</b>
<b>C. Femtosecond Laser Ablation</b>	<b>39</b>
C.1. Generation of femtosecond laser pulses . . . . .	39
C.2. Ultrashort-pulse laser ablation . . . . .	39
<b>D. Discrete Dipole Approximation</b>	<b>42</b>
<b>E. Finite Integration Technique</b>	<b>47</b>
<b>References</b>	<b>51</b>

## Introduction

Nanophotonics is a field that studies light manipulation at the nanoscale — using various nanostructures to control the propagation of light. Nanophotonic devices can range from relatively simple perfect reflectors/absorbers to optical computers. Applications include antireflective coatings for solar cells, all-optical switching for optical telecommunications, and various medical sensing tasks.

Traditionally nanophotonic devices have utilized plasmonic nanostructures. Plasmonic metallic nanoparticles have very strong electric dipole resonances, meaning that they readily interact with the electric component of electromagnetic fields. Problems arise when one tries to control the magnetic component of electromagnetic fields, because plasmonic nanoparticles do not have an inherent magnetic dipole response. A solution is the split-ring resonator — a nanostructure with a magnetic dipole response. Having building blocks to control both the electric and magnetic components of electromagnetic fields, plasmonic structures have been efficiently used in frequency ranges from gigahertz to several hundred terahertz — up to infrared wavelengths. But, because of strong losses in the optical spectral range, and of the complexity of fabricating split-ring resonators for optical wavelengths, plasmonics have had a lot of difficulty in achieving the required performance for optical nanophotonic devices.[63]

This is where the concept of dielectric nanophotonics comes into play. Mie theory predicts[36] and it has been experimentally demonstrated[35] that dielectric nanoparticles have both electric and magnetic resonances. The positions of the resonances are size and shape dependent, making them easily tunable for any wavelength. Crystalline silicon has proven itself as a good material for dielectric nanophotonics — low losses at optical wavelengths[45], high refractive index, and compatibility with many fabrication processes[49, 37, 44, 56, 1, 53, 11, 63].

Dielectric nanoparticles have been used for sensing and electromagnetic field enhancement [33, 71, 34, 43], antireflective coatings[55], perfect reflectors[44, 15], light wavefront manipulation[23, 24], superdirective scattering[58, 16] and enhancement of nonlinear effects[14, 64].

# 1 Dielectric Nanophotonics

## 1.1 Crystalline Silicon as the Material of Choice for Dielectric Nanophotonics

Crystalline silicon has been almost ubiquitously chosen as the material of choice for dielectric nanophotonics. There are several reasons for this. First, the material parameters are suitable for visible and infrared nanophotonic devices — Crystalline silicon has a high refractive index,  $n \approx 3.5$  at visible and IR wavelengths[30], giving high contrast with air, and therefore good field confinement for resonant particles at those wavelengths[36, 54]. Also a very important fact, distinguishing crystalline silicon from amorphous silicon, is the near-zero absorption at visible wavelengths, meaning that crystalline silicon nanoparticles are nearly lossless at visible and IR wavelengths, making any potential nanophotonic devices very efficient and not prone to thermal dissipation — something that plagues their plasmonic counterparts. Silicon, being the basis of almost all modern electronics, can easily boast a highly developed ecosystem of fabrication and processing technologies, making it very easy (if expensive) to fabricate almost any required structure. **Last, but not least, silicon is a bio-compatible material, meaning it is easy to design nanophotonic devices for medical applications.**

Another interesting application dimension is related to the existence of an intrinsic Raman response in crystalline silicon. Raman scattering of light, and inelastic scattering phenomenon, is an important electromagnetic effect[22] that has a large number of applications: sensing[39], optical amplification[26], lasing[47]. Traditionally, enhancement of Raman scattering for SERS applications has been mostly delegated to metallic nanoparticles, but recent studies of high-index subwavelength nanoparticles have paved the way for all-dielectric resonant nanophotonic devices, including the possibility of enhancing Raman scattering, including intrinsic Raman from the nanoparticles.

## 1.2 Analytical Models

### 1.2.1 Mie-Type Resonances of Dielectric Nanoparticles

An important problem for dielectric nanophotonics is the scattering of electromagnetic radiation by a homogeneous sphere. This problem has an analytical solution, generally called Mie theory[36]. The solution of this problem utilizes the symmetry of the problem, and decomposes the scattered radiation into vector spherical harmonics. The result is a set of coefficients,  $a_i, b_i$  describing the relative contributions of  $a_i$ , electric multipole resonances and  $b_i$ , magnetic multipole resonances into the final scattered field.

Based on this, one can easily estimate the extinction, scattering and absorption cross-sections (for a detailed derivation, see Appendix A):

$$C_{sca} = \frac{2\pi}{k_m^2} \sum_{l=1}^{\infty} (2l+1)(|a_l|^2 + |b_l|^2) \quad (1)$$

$$C_{ext} = \frac{2\pi}{k_m^2} \Re \sum_{l=1}^{\infty} (2l+1)(a_l + b_l) \quad (2)$$

$$C_{abs} = C_{ext} - C_{sca} \quad (3)$$

The main limitation of the Mie solutions is their reliance on the symmetry of the scatterer — the solution can be generalized to layered spheres, layered infinite cylinders, but scatterers lacking symmetry cannot be accurately described by Mie-type solutions. In those cases, T-Matrix methods can be used, but they are outside the scope of this thesis.

### 1.2.2 Raman Scattering from Crystalline Materials

Raman scattering of light from crystalline materials is inelastic scattering resulting from the interaction of optical phonons with the incident light. Raman scattering is a versatile method of probing the phonon structure of the materials. A simplistic classical model of Raman scattering is sufficient to demonstrate the effect and to properly predict many of the Raman scattering peaks of semiconductors[48]. In the model, interaction between light and phonons is represented as a perturbation of the electric susceptibility  $\chi$ :

$$\chi(\vec{k}_i, \omega_i, \vec{Q}) = \chi_0(\vec{k}_i, \omega_i) + \frac{\partial \chi}{\partial \vec{Q}_0} \vec{Q}(\vec{r}, t) + \dots \quad (4)$$

Where  $Q$  represents the displacement of atoms in the lattice by phonons. Then the induced polarization by the incident light, perturbed by the phonons can be written as

$$\vec{P}_{ind}(\vec{r}, t, \vec{Q}) = \frac{\partial \chi}{\partial \vec{Q}_0} \vec{Q}(\vec{r}, t) \vec{F}_i(\vec{k}_i, \omega_i) \cos(\vec{k}_i \cdot \vec{r} - \omega_i t) \quad (5)$$

which contains both Stokes and anti-Stokes shifted components. The intensity of the Raman scattered light is dependent on the polarization of the incident light and the phonon structure of the material. All of this information can be condensed into a second rank Raman tensor:

$$\hat{R} = \frac{\partial \chi}{\partial \vec{Q}} \vec{Q}_n \quad (6)$$

$$I_s \propto |\vec{e}_i \cdot \hat{R} \cdot \vec{e}_s|^2 \quad (7)$$

A more detailed derivation can be found in Appendix B.

## 1.3 Numerical Models

Since scattering from arbitrarily-shaped particles cannot be analytically described, use of numerical modeling methods is required to model these particles. A large number of numerical methods exist that can be used for these purposes.

### 1.3.1 Discrete Dipole Approximation

The discrete dipole approximation (DDA) is a method of numerically simulating light scattering from arbitrarily shaped particles. The general idea of the method is to replace an arbitrarily shaped scatterer by a set of point dipoles and calculate the scattering by each dipole on its own plus the interaction between the dipoles. This makes calculations straightforward for scatterers of arbitrary geometries and compositions. Using this assumption, the extinction and absorption cross-section are represented by simple sums, iterating over all of the point dipoles, using the polarization of each dipole and the field at the location of the dipole:

$$C_{abs} = 4\pi k \sum_i V_i \Im(\chi_i) |\vec{E}_i|^2 = 4\pi k \sum_i \Im(\vec{P}_i \vec{E}_i^*) \quad (8)$$

$$C_{ext} = 4\pi k \sum_i \Im(\vec{P}_i \cdot \vec{E}_i^{inc*}) \quad (9)$$

The main disadvantage of this method is staircase errors, caused by based approximation of ellipsoidal boundaries by a point-dipole model on a Cartesian grid. The only real solution is to increase the number of dipoles used to simulate the scatterer, which quickly increases computation time. Another difficulty is including surface interaction, which adds another interaction term to the solution, and further complicates the computation. A detailed derivation of the basic DDA is provided in Appendix D.

### 1.3.2 Finite Element Method

The Finite Element Method (FEM) is a numerical technique, first introduced in the 1940s[7], to find approximate solutions to boundary-value problems. The technique has been used in many fields, from mechanical structure problems to electromagnetic field propagation. The idea of the method is to replace a continuous domain by a number of sub-domains, in each of which the solution is approximated by interpolation functions. A linear system of algebraic equations is obtained by applying continuity boundary conditions on the internal sub-domains and problem-specific boundary conditions on the external subdomains. The system can then be solved by any solver for linear systems. The subdomains are generally chosen to be tetrahedra or hexahedra for three-dimensional solutions with the internal fields approximated by piecewise polynomial functions, but, in general, the method has no limitations on the shape and size of the subdomains and the approximation functions inside each of the subdomains. This allows the method to accurately model complicated

scattering geometries. The flip side of this flexibility — large space requirements for the system of equations. The method also often requires iterative refinement of the grid to achieve good convergence.

### 1.3.3 Finite Difference Time Domain

The Finite Difference Time Domain (FDTD) method is very straightforward technique to solve the propagation of electromagnetic radiation, first developed by Yee[69]. The method approximates both spatial and temporal derivatives in the Maxwell's equations by finite-difference expressions. The standard implementation does this on a staggered Cartesian grid, with the electric field defined on one sub-grid and the magnetic field defined on the second sub-grid. This results in a system of linear equations, where each time step is used to calculate the electric field on the first sub-grid from the magnetic field on the second sub-grid, and then the magnetic field at the next time step from the electric field, and so on, until a termination condition is reached. The main advantage of this method is its simplicity — no matrix solvers required, possibility for very efficient implementations. The disadvantage is that this simplicity makes the method very rigid in terms of time step and spatial step choices for good convergence, to mitigate staircase-type errors caused by inefficient mapping of complex scatterer geometry onto a Cartesian grid.

### 1.3.4 Finite Integration Technique

The Finite Integration Technique (FIT)[67], is ideologically similar to the FDTD method, but works with the integral formulation of Maxwell's equations instead of the derivative formulation used by the FDTD. This grants the method more flexibility in grid geometry, allowing for more accurate modeling of complicated scatters. The accuracy of the method, like with FDTD, is still highly dependent on the choice of grid size and time step. A detailed derivation for a simplistic case, with a Cartesian grid, can be found in Appendix E.

## 1.4 Fabrication of Dielectric Nanoparticles

There are several techniques to fabricate dielectric nanoparticles. They can be ordered in terms of level of control over the size of the particles and the options of building patterned nanostructures for the nanoparticles. Complexity and cost of the processes generally correlate with the level of control provided by the different techniques. The main techniques can be grouped into: chemical synthesis[41], thin-film dewetting[65], laser ablation-based[29] and lithographic methods.

### 1.4.1 Chemical Synthesis

Chemical vapor deposition of silicon from disilane gas has been used to fabricate silicon nanoparticles, ( $Si_2H_6 \rightarrow 2Si + 3H_2$  at high temperatures) achieving polycrystalline spherical particles[41]. Monodisperse colloidal particles have been fabricated from trisilane ( $Si_3H_8$ ) at high temperature

in n-Hexane[38]. Sizes of the particles were controlled by changing the concentration of the trisilane and the temperature of the reaction. The main disadvantages of these types of methods are the porosity and high hydrogen concentration of the particles and necessity of further processing if ordered nanostructures are required.

#### **1.4.2 Thin-Film Dewetting**

Thermal dewetting of thin films can be used to create arrays of nanoparticles, with size and phase controlled by the thickness of the initial film and temperature of the process[65]. If fabricated from an unpatterned film, the particles will be unordered — producing ordered particles is this way requires an additional patterning of the the film, usually by lithographic processes, which increases the complexity of the process and the cost.

#### **1.4.3 Laser Ablation-Based Methods**

Laser ablation by focused ultra-short pulses can also be used to fabricated nanoparticles by heating up the irradiated area to eject material into spherical particles deposited either near the irradiated area[35] or transferred to another substrate[29]. Control of the beam sport, fluency and donor material structure and be used to control individual particle size and the number of particles fabricated from a single pulse (down to one particle in best-case scenario). The ultra-short pulses can also be used to change the phase of already fabricated structures by means of light-induced thermal annealing. The main advantage of femtosecond laser ablation is th ability to gently remove material from the surface — allowing for very precise and controllable modification of the surface or precise and controllable formation of nanoparticles. Femtosecond laser ablation is a complicated process that requires complex 3D simulations to accurately predict the outcome of the light-material interaction. A simple qualitative description is provided in Appendix C

The shortcomings of the current methods are that they often require additional annealing to crystallize the fabricated nanoparticles and that method presented in [29] is limited to transferring nanoparticles to transparent substrates.

#### **1.4.4 Lithographic Methods**

Using electron beam lithography and reactive ion etching, one can pattern substrates with high-quality nanocylinders, with near-perfect control of both size and positioning of the structures[34]. This give great flexibility in terms of fabricating ordered nanostructures, but at the cost of extreme complexity and high costs.

## 1.5 Experimental Characterization Methods

### 1.5.1 Electron Microscopy

Electron microscopy is a very high-resolution, down to single nanometer resolutions, method to probe geometrical and material parameters of structures. The structure is probed by a focused electron beam, measuring either scattered or transmitted primary electrons, secondary electrons or emitted photons. Because of charge accumulation caused by the electron beam, samples usually need to be conductive to facilitate charge draining, or else the resulting signal will be distorted. The two main methods used are scanning electron microscopy (SEM) and transmission electron microscopy (TEM).

#### 1.5.1.1 Transmission Electron Microscopy

In TEM, a collimated high-voltage electron beam, is used to illuminate the specimen. The transmitted beam is then projected, with magnification, onto a viewing screen. The transmitted electron beam contains information on the material properties of the sample, based on the interaction of the electrons in the beam with the sample.

This type of microscopy can achieve sub-nanometer resolutions, and can be used to probe different phases of materials, see different grains of polycrystalline materials and even visualize crystalline defects such as dislocations.

The main difficulty related to TEM is the complicated sample preparation — good TEM samples should be around 100nm thick, for optimal electron-sample interaction.

#### 1.5.1.2 Scanning Electron Microscopy

In SEM, a focused electron beam illuminates a small portion of the sample, and the image of the sample is formed by collecting either back-scattered electrons, secondary electron, Auger electrons or characteristic X-Rays. Depending on what signal is collected, different information about the sample is obtained, e.g. different types of signals originate from different interaction volumes, giving differing information of about bulk or surface sample composition.

Secondary electrons originate from within a few nanometers of the surface, giving good topographical information.

Backscattered electrons also give information about chemical composition, since heavier elements backscatter electrons more strongly, with those areas appearing brighter in the final image.

### 1.5.2 Optical Characterization

The scattering properties of nanostructures (in the visible spectral range) can be measured by relatively simple optical measurements. A very good method for measuring elastic scattering is dark field microscopy, where the only collected signal is the light scattered by the structure. Inelastic

scattering often means either Fluorescence measurement or Raman scattering. In the first shorter wavelength light is absorbed by the sample and then re-emitted as longer wavelength light, usually with rather large shifts in wavelength, making measurements relatively easy. Raman scattering, on the other hand, is usually much weaker than the excitation signal, and spectrally very close to the excitation signal, making it relatively difficult to single out.

#### 1.5.2.1 Elastic Scattering — Dark Field Microscopy

Dark field microscopy has the excitation source angled to the surface of the sample substrate in such a way, that none of the reflected excitation illumination can enter the collection channel. In terms of objective numerical apertures this means that the excitation source is at an angle larger than the critical angle of the collection channel objective. The only light that is collected by the collection objective is light scattered from the sample. This allows for direct measurement of the scattering properties of the sample. A schematic of such a system can be seen in Figure 2 in the next chapter.

This is usually used to measure elastic scattering — the collected scattered light is the same wavelength as the excitation.

#### 1.5.2.2 Inelastic Scattering — Raman Scattering

Fluorescence microscopy and Raman scattering involve measuring scattered light at a wavelength that is different from the wavelength of the excitation. This generally requires filtering out the excitation wavelengths, and is especially important for Raman measurements, where the wavelength shift between the excitation and scattered is very small. A schematic of such a system can be seen in Figure 2 in the next chapter.

### 1.5.3 Scanning Probe Methods

Another class of characterization methods exist that can probe the geometrical and electromagnetic properties of nanostructures. These include techniques like atomic force microscopy (AFM) to probe geometrical properties and near-field scanning optical microscopy (NSOM), which can be used to probe electromagnetic field modes close to the structures.

## 1.6 Goals

The project was devoted to the fabrication as well as the characterization of elastic and inelastic scattering from resonant crystalline silicon nanoparticles.

The goals of this project were to:

- Implement the Discrete Dipole Approximation method to calculate scattering cross-sections of dielectric particles

- Develop a simple, single-stage femtosecond laser ablation method of fabricating crystalline silicon nanoparticles
- Carry out optical characterization through single-particle polarization-resolved scattering experiments
- Determine the sizes of the particles based on the spectral positions of the Mie-type resonances of the particles
- Perform single-particle Raman spectroscopy experiments to prove crystallinity
- Study the influence of Mie resonances on Raman scattering from particles.

## 2 Methods

### 2.1 Fabrication of Crystalline Silicon Nanoparticles by Femtosecond Laser Ablation

The first part of the project was to develop a new, simple, method of fabricating crystalline dielectric nanoparticles. The idea was to use controlled laser ablation — a very simple technique — to produce the particles. Previous work on the topic[35, 29] has shown that it is possible to fabricate single particles of a certain size.

We ended up developing two different methods to fabricate crystalline nanoparticles — direct laser writing of crystalline nanoparticles out of a thin film of amorphous silicon (adapted from a method used for plasmonic nanoparticles[6, 10]), and a forward transfer of nanoparticles by single femtosecond laser pulses from a transparent substrate with a thin film of amorphous silicon to an arbitrary acceptor substrate. The second method is similar to the one presented in [29], but does not require any additional annealing steps to achieve nanoparticle crystallinity and is not limited to transparent acceptor substrates.

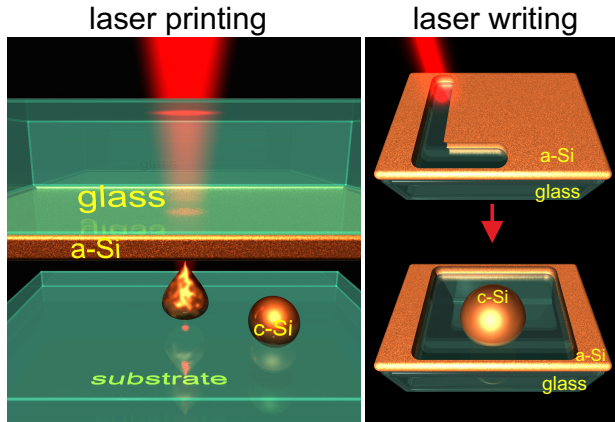


Figure 1: Geometry of laser-ablation based fabrication methods of crystalline nanoparticles from amorphous thin films.

#### 2.1.1 Laser Transfer of Crystalline Dielectric Particles

Single laser pulses were selected by a Pockels cell-based pulse picker (also Avesta Project), focused by an oil immersion microscope objective (Olympus 100 $\times$ ) with a numerical aperture of  $NA = 1.4$ . According to the relation  $d \approx 1.22\lambda/NA$ , the estimated diameter of the beam's focal spot size was  $d = 0.7 \mu\text{m}$ , which was close to the value measured by a method based on the dependence of the laser-damaged area on incident laser energy ( $0.68 \mu\text{m}$ ) [31]. The nanoparticles were fabricated from an 80 nm thick a-Si:H film deposited on a fused silica substrate by plasma enhanced chemical vapor deposition from a SiH<sub>3</sub> precursor gas.

The nanoparticles were fabricated by single laser pulses (from a previously undamaged surface of the a-Si:H film) in a forward-transfer geometry, where the receiving substrate is placed under the film with a spacing of  $\sim 50 \mu\text{m}$  (figure 1(a)). This geometry has an advantage over the back-transfer geometry used in [29], because of the possibility of transferring nanoparticles onto a wide variety of substrates, including opaque and structured samples.

The silicon nanoparticles were printed at laser energies in the range of  $0.5 - 1.2 \text{ nJ}$ , providing fluencies in the range of  $0.12 - 0.16 \text{ J/cm}^2$ . The fabricated nanoparticles were almost spherical in shape(figure 8(b)) and their diameters lie in the range of  $50 - 200 \text{ nm}$ , depending on the fluence.

### 2.1.2 Laser Writing of Dielectric Particles

The direct laser writing of crystalline Si nanoparticles was carried out from an initially amorphous a-Si:H film. The process consists of using a train of femtosecond pulses to cut patches out of the a-Si thin film[6, 10]. A laser fluence  $F \approx 100 \text{ mJ/cm}^2$  provides film heating close to the melting point even in a single shot regime, while a pulse train with a  $12.5 \text{ ns}$  delay between pulses leads to the temperature accumulation and exceeding of the ablation threshold. The heat transferring from the ablated area to the surrounding film is accumulated much stronger in the cut patches, which are thermally isolated from the rest of the film. These micro-patches are unstable at high temperatures and undergo dewetting to a certain number of similar nanoparticles [62].

## 2.2 Optical Measurements

All of the optical characterization measurements were carried out on a multifunctional setup, depicted in Fig. 2. The setup allowed us to measure optical signals from single nanoparticles, provided that there was at least  $1\mu\text{m}$  between the nanoparticle and its nearest neighbors. The XYZ-stage used for the positioning of the particles had 100nm precision, giving enough control to position a single nanoparticle into the center of the excitation beam.

The scattered light was collected from the top by an objective (Mitutoyo M Plan APO NIR, 100x, NA=0.7), sent to a Horiba LabRam HR spectrometer and projected onto a thermoelectrically cooled charge-coupled device (CCD, Andor DU 420A–OE 325) with a 150-g/mm diffraction grating. The spectrometer gave us a spectral resolution of around 1nm.

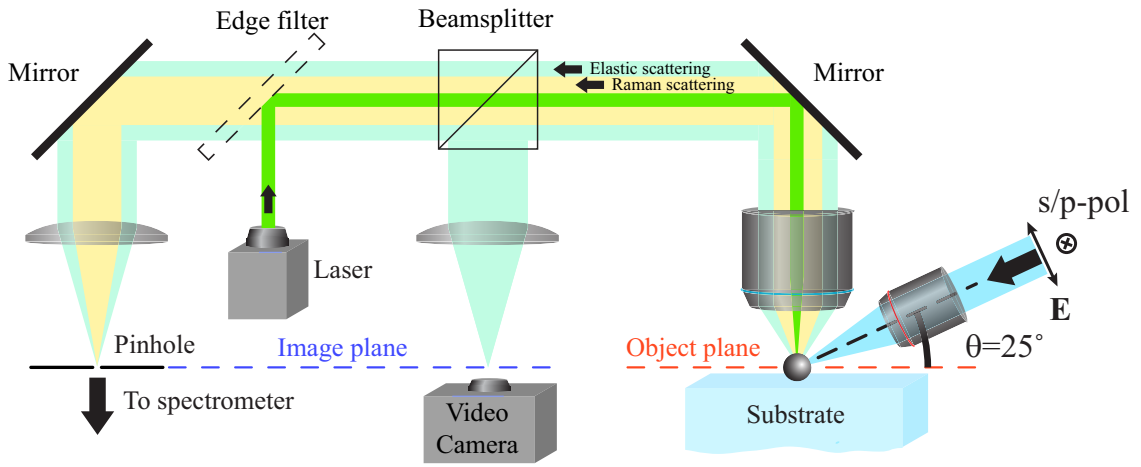


Figure 2: Schematic of the experimental setup used for all of the optical measurements.

### 2.2.1 Polarization-Resolved Dark-field Spectroscopy of Single Nanoparticles

For the dark-field scattering experiments, the nanoparticles were excited at an oblique angle of incidence (65 degrees to the surface normal) by linearly polarized light from a halogen lamp (HL-2000-FHSA) through a weakly-focusing objective (Mitutoyo M Plan Apo NIR, 10x, NA=0.28). The polarization allowed us to selectively excite different modes in the nanoparticles[50].

### 2.2.2 Raman Spectroscopy of Single Nanoparticles

For the Raman scattering experiments, the nanoparticles were excited by one of two laser sources: a 632.8nm HeNe laser or a 532nm Nd:YAG laser, through the same channel that was used to collect the scattered light. A lowpass filter was used to filter out the excitation wavelength and leave only the Stokes-shifted inelastically scattered light.

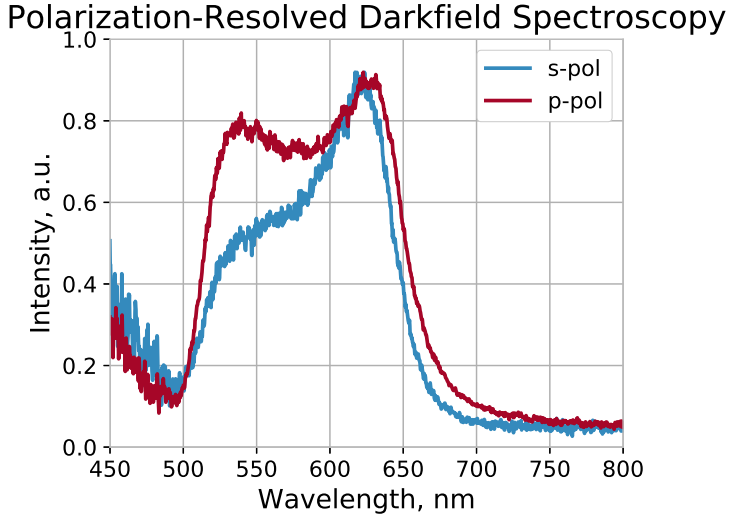


Figure 3: Different Mie-type resonances excited by different polarizations of incident light.

## 2.3 Analytical Model of Raman Signal Enhancement by Mie resonances of Nanoparticles

This derivation is based on the derivation from [54].

To describe the enhancement of Raman scattering and analyze the role of the electric and magnetic Mie resonances of a silicon nanoparticle, we employ the rigorous Green tensor approach. Ideologically, our theoretical approach is based on earlier related studies [60, 40].

In this framework, we first determine the spatial field distribution  $\mathbf{E}_{exc}(\mathbf{r})$  inside the nanoparticle at the excitation frequency created by an external source. Assuming that a spherical nanoparticle in free space is illuminated by a plane wave, we represent the normalized electric field inside the nanoparticle as a series of vector spherical harmonics [3]:

$$\mathbf{E}_{exc}(\mathbf{r}) = \sum_{n=1}^{\infty} E_n \left( c_n \mathbf{M}_{o1n}^{(1)}(\mathbf{r}) - id_n \mathbf{N}_{e1n}^{(1)}(\mathbf{r}) \right), \quad (10)$$

where  $c_n$  and  $d_n$  are the Mie coefficients,  $\mathbf{M}_{o1n}^{(1)}$  and  $\mathbf{N}_{e1n}^{(1)}$  are the orthogonal vectorial spherical harmonics, and  $E_n = i^n(2n+1)/[n(n+1)]$ . The excitation field distribution at each point inside the medium defines the Raman polarization oscillating at the Stokes frequency  $\omega_S$  according to

$$\mathbf{P}_s(\mathbf{r}) = \chi_s \hat{\alpha}_j(\mathbf{r}) \mathbf{E}_{exc}(\mathbf{r}), \quad (11)$$

where  $\chi_s$  is the scalar Raman susceptibility, and  $\hat{\alpha}_j$  is the Raman polarizability tensor representing the threefold degenerate transverse optical (TO) phonon mode excitation [52, 48]. Induced Raman polarization, in turn, produces an electromagnetic field at the observation point  $\mathbf{r}_0$  given by  $\mathbf{E}_s(\mathbf{r}_0) = (\omega_s^2/c^2) \int_V \hat{G}_s(\mathbf{r}_0, \mathbf{r}) \mathbf{P}_s(\mathbf{r}) d^3\mathbf{r}$ , where  $\hat{G}_s(\mathbf{r}_0, \mathbf{r})$  is the Green tensor at the Stokes frequency accounting for the Si nanoparticle and integration is carried out over the nanoparticle

volume  $V$ . Finally, the collected signal at the point  $\mathbf{r}_0$  is presented in the form:

$$S(\mathbf{r}_0) = \sum_j \langle \mathbf{E}_s^*(\mathbf{r}_0) \mathbf{E}_s(\mathbf{r}_0) \rangle = \sum_j \frac{\omega_s^4}{c^4} \iint_V d^3\mathbf{r}_1 d^3\mathbf{r}_2 \left\langle \hat{G}_s^*(\mathbf{r}_0, \mathbf{r}_1) \mathbf{P}_s^*(\mathbf{r}_1) \hat{G}_s(\mathbf{r}_0, \mathbf{r}_2) \mathbf{P}_s(\mathbf{r}_2) \right\rangle \quad (12)$$

$$= \sum_j \frac{\omega_s^4}{c^4} \iint_V d^3\mathbf{r}_1 d^3\mathbf{r}_2 \hat{G}_s^*(\mathbf{r}_0, \mathbf{r}_1) \mathbf{E}_{exc}^*(\mathbf{r}_1) \hat{G}_s(\mathbf{r}_0, \mathbf{r}_2) \mathbf{E}_{exc}(\mathbf{r}_2) \chi_s^2 \langle \hat{\alpha}_j^*(\mathbf{r}_1) \otimes \hat{\alpha}_j(\mathbf{r}_2) \rangle, \quad (13)$$

where summation is performed over the three degenerate TO phonon modes. Since the Raman scattering is a spontaneous process (until we enter the stimulated Raman scattering regime), the induced polarization  $\mathbf{P}_s$  is not coherent across the whole particle. Therefore, in Eq. (13), the averaging is carried out over all possible realizations of the Raman polarization  $\mathbf{P}_s$ . Taking into account that the correlation length of the Raman scattering in silicon  $L_c$  is of the order of tens nanometer and much less than the nanoparticle diameter, we approximate the correlation of the Raman polarizability tensors by the Dirac delta function  $\langle \hat{\alpha}_j(\mathbf{r}_1) \otimes \hat{\alpha}_j(\mathbf{r}_2) \rangle \sim \delta(\mathbf{r}_1 - \mathbf{r}_2)$ . Under this assumption, Eq. (13) reduces to

$$S(\mathbf{r}_0) = \frac{\omega_s^4}{c^4} \sum_j \int_V d^3\mathbf{r} \left| \hat{G}_s(\mathbf{r}_0, \mathbf{r}) \hat{\alpha}_j \chi_s \mathbf{E}_{exc}(\mathbf{r}) \right|^2 \quad (14)$$

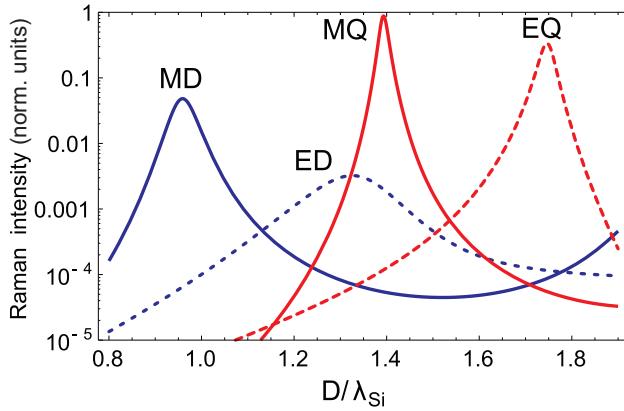


Figure 4: Log plot of normalized intensity of Raman scattering as a function of dimensionless nanoparticle diameter for the magnetic dipole (MD), electric dipole (ED), magnetic quadrupole (MQ) and electric quadrupole (EQ) resonances.

Expression (14) can be simplified with the use of the single-mode approximation. First, we notice that the electromagnetic response of an optically small Si nanoparticle at the excitation wavelength is dominated by a single magnetic or electric multipole resonance depending on the particle radius [44]. Therefore, we can keep only one resonant term in Eq. (10) and represent the electric field inside the nanoparticle as  $\mathbf{E}_{exc} \approx E_n c_n \mathbf{M}_{o1n}^{(1)}$ , for the  $n$ -th magnetic resonance, and  $\mathbf{E}_{exc} \approx -i E_n d_n \mathbf{N}_{e1n}^{(1)}$ , for the  $n$ -th electric resonance, respectively. Furthermore, since the Raman

shift in silicon is small compared to the linewidth  $\gamma$  of Mie resonance at  $\omega_0$ , the main contribution to the Green tensor is provided by the same eigenmode of the system. Therefore, expanding the Green tensor in the series of eigenmodes [25] and keeping only the resonant term, we obtain

$$\hat{G}_s(\mathbf{r}_0, \mathbf{r}) \approx \frac{c^2}{N^2} \frac{\mathbf{u}(\mathbf{r}_0) \otimes \mathbf{u}^*(\mathbf{r})}{(\omega_0 + i\gamma)^2 - \omega_s^2}, \quad (15)$$

where  $\mathbf{u}(\mathbf{r})$  is the spatial field distribution of the eigenmode, and  $N^2 = \int \text{Re}\epsilon(\mathbf{r}) |\mathbf{u}(\mathbf{r})|^2 d^3\mathbf{r}$  is the normalization constant. Finally, integrating the expression (5) over the whole volume  $V$  of the nanoparticle, we arrive at the following simple expression describing the Raman signal enhanced by a single Mie resonance:

$$S(\mathbf{r}_0) \approx V \left( \frac{\omega_s}{c} \right)^4 \left| \frac{\chi_s s_n}{(\omega_0 + i\gamma)^2 - \omega_s^2} \right|^2, \quad (16)$$

where  $s_n$  stands for the Mie coefficient, either  $c_n$  or  $d_n$  of the corresponding mode. The above expression clearly shows that the total enhancement of Raman scattering depends on two factors: the enhancement of the excitation field inside the medium, and the Purcell enhancement of the Raman dipoles radiation [9].

The two key parameters entering Eq. (16) are the resonance frequency  $\omega_0$  and the resonance linewidth  $\gamma$ . The resonance frequency can be easily estimated numerically, while for the estimation of the resonance linewidth one can employ analytical expressions from Ref. [12]. Substituting these values into Eq. (16), we obtain the desired spectrum of Raman scattering enhanced by the resonances of a silicon sphere. This spectrum (normalized by the particle volume  $V = 4\pi R^3/3$ ) is plotted in Fig. 4 as a function of dimensionless nanoparticle diameter  $D/\lambda_{\text{Si}}$  with  $\lambda_{\text{Si}} = 163$  nm being the wavelength of the excitation signal inside the silicon for the magnetic dipole (MD), electric dipole (ED), magnetic quadrupole (MQ) and electric quadrupole (EQ) resonances assuming a constant excitation wavelength of 633 nm, used below in experiments.

The derived single-mode expression (16) allows us to clearly separate contributions of each Mie resonance of the nanoparticle into the total Raman scattering enhancement. As follows from Fig. (4), the strongest enhancement is associated with the MQ resonance due to its high  $Q$ -factor. Notably, the predicted Raman scattering enhancement at the MD resonance, which occurs for the smallest particles, is more than an order of magnitude larger than that for the ED resonance.

### 2.3.1 Numerical Methods

Several numerical methods were used to simulate the scattering properties of the fabricated nanoparticles — to prove their crystalline phase, to probe their shape, to determine their size. The initial idea was to use the Discrete Dipole Approximation, because it is very flexible and can work with scatterers of arbitrary geometry. The main problem we encountered was the fact the method is very involved (especially if one tries to incorporate substrate interaction), and computationally intensive for the required problems. Many calculations turned out to be excessive — a simple Mie

theory calculation, while simulating the incorrect geometry, was more than enough to model the required parameters, with error well within the requirements.

For calculations of field distribution inside the nanoparticles presented in this thesis, CST Microwave Studio was used. It is an EM simulation package that uses the Finite Integration Technique for most of its calculations.

### 2.3.2 Discrete Dipole Approximation

For the DDA calculations, a custom, Python-based implementation was written, PyDDA — a reimplementation of an existing Matlab toolkit, DDA-SI[32]. The implementation even included surface-interaction components in its' calculations, but the complexity of the calculation and difficulty of accurately modeling particles led to the DDA being abandoned in favor of plain Mie theory, which provided more than enough accuracy for the purposes of the project.

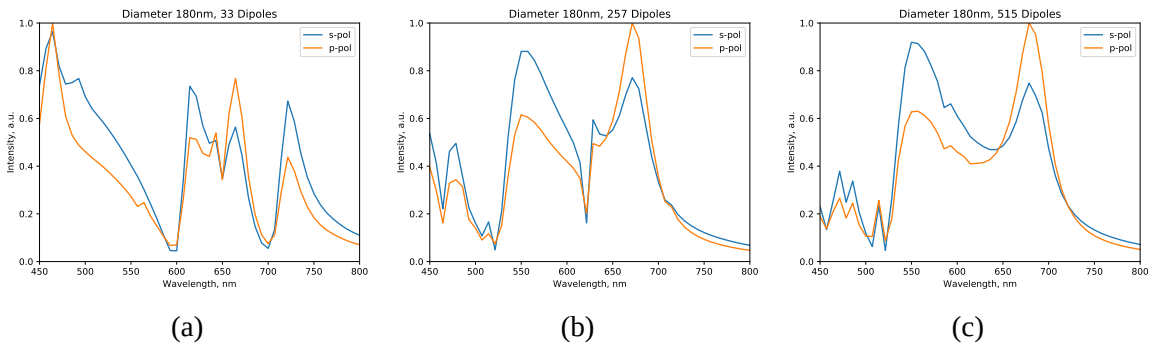


Figure 5: Scattering from isotropic sphere modeled by DDA using a) 33, b) 257, c) 515 dipoles to model the sphere.

### 2.3.3 Finite Integration Technique

CST Microwave studio was used to model field distribution inside and around the silicon nanoparticles, to demonstrate the electric field confinement at different types of resonances (electric and magnetic dipole resonances). The model was a slightly oblate spheroid, corresponding to the experimentally determined geometric parameters of the nanoparticles.

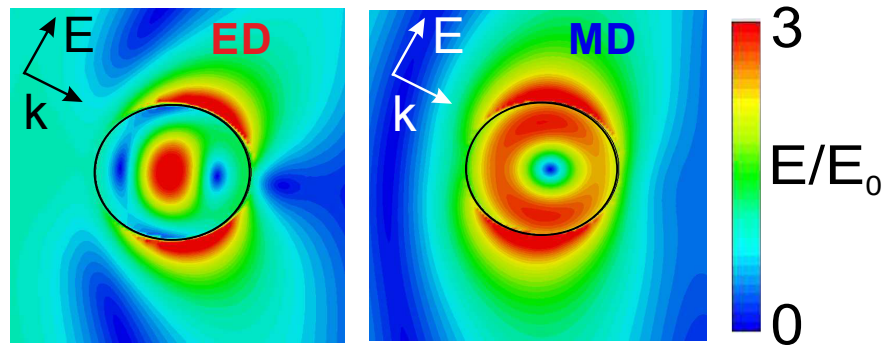


Figure 6: Field distribution inside 180nm spheroid nanoparticle with 1.12 oblateness parameter at electric and magnetic dipole resonances, calculated using CST Microwave Studio

### 3 Experimental Results

#### 3.1 Fabrication of Crystalline Silicon Nanoparticles

##### 3.1.1 Laser Writing of Nanoparticles

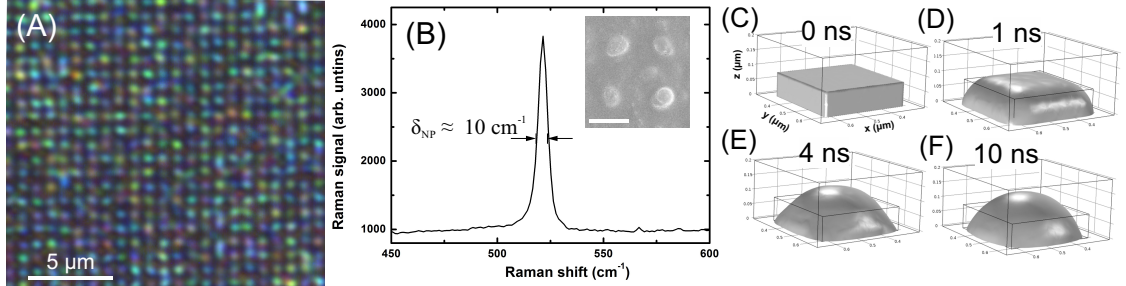


Figure 7

As we have shown, the laser [transfer](#) method allows to fabricate c-Si nanoparticles with distinguished resonances, however it does not allow to obtain an ordered array of nanoparticles from the amorphous film similarly to the previously published results on bulk c-Si [19]. Therefore, we develop a novel method of direct laser writing of c-Si resonant nanoparticles via cutting of submicron square patches by the fs-laser irradiation at a 80 MHz repetition rate (Fig. 7A). At scanning velocity of 1 mm/s and laser fluence of  $\approx 100 \text{ mJ/cm}^2$ , narrow (width of  $\approx 300 \text{ nm}$ ) grooves can be written directly in the a-Si:H film.

Under the optimal conditions of fabrication the resulting array of nanoparticles has a period of about  $0.9 \mu\text{m}$ , exhibiting bright colors originating from the resonant scattering (Fig. 7A). Though the cutting should produce an array of square patches, our SEM images show that the nanoparticles look almost circular from the top (Fig. 7B). This is due to thermal isolation of the patch from the rest of the film and its overheating during the cutting by a train of femtosecond laser pulses with the period of 12.5 ns. These microscale patches are known to be unstable at high temperatures and undergo dewetting to a certain number of similar nanoparticles depending on their dimensions [62]. In order to provide deeper insight into the mechanism of the patches reshaping, we model the time dynamics of the cut liquid silicon patch with the height of 80 nm and similar widths of 300 nm (Figs. 7C) on a fused silica substrate in the COMSOL software, solving the incompressible Navier-Stokes equations and taking into account the parameters of the used materials. The modeling shows that after ten nanoseconds the patch is transformed into the hemisphere with a height of about 140 nm and width of about 350 nm (Figs. 7C-F), giving qualitative agreement with the experimentally observed shapes.

The corresponding Raman signals from these nanoparticles also reveal the crystalline state of the nanoparticles written by the laser, demonstrating a narrow peak at  $520 \text{ cm}^{-1}$ , with a half-width

of about  $10 \text{ cm}^{-1}$  (Fig. 7B), which is larger than the half-width of the printed nanoparticles about  $4-5 \text{ cm}^{-1}$ . The larger half-width corresponds to the smaller mean crystallite size, i.e. less than  $10 \text{ nm}$  according to the previous studies [5]. The origin of this difference is related to the faster cooling rate for the written nanoparticles on the fused silica substrate as compared with nanoparticles flying in air before deposition in the [transfer](#) mode, owing to the 20-fold larger value of the glass thermal conductivity in comparison with that one for air.

### 3.1.2 [Laser Transfer of Nanoparticles](#)

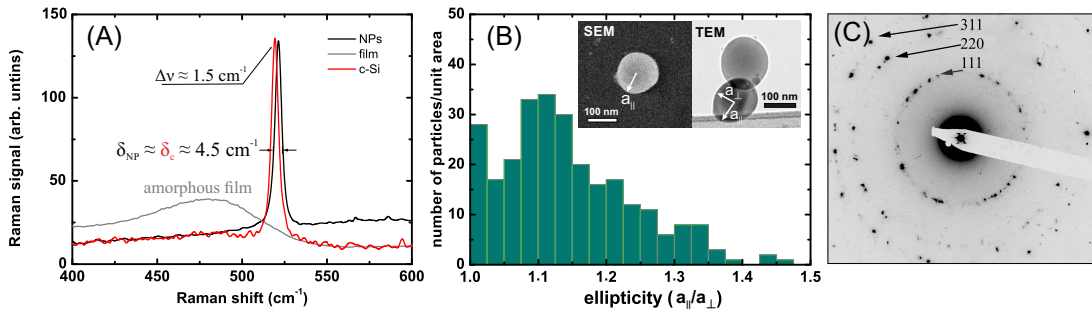


Figure 8

Scanning electron microscopy (SEM, Carl Zeiss, Neon 40), registering backscattered electrons, was used determine the geometrical parameters of the nanoparticles. In particular, that the particles possess [axial](#) symmetry along the substrate normal (Fig. 8B).

We characterized the initial a-Si:H film revealing its amorphous state from the observation of its broad Raman peak centered around  $480 \text{ cm}^{-1}$ . The measured Raman spectra from individual nanoparticles have narrow peaks at  $521.5 \text{ cm}^{-1}$ , corresponding to the crystalline cubic diamond structure. The reference Raman signal from a bulk crystalline silicon wafer and the literature data say that the Raman peak of pure crystal corresponds to  $520 \text{ cm}^{-1}$ . The slight positive shift of the peak of the nanoparticles  $\Delta\nu = 1.5 \text{ cm}^{-1}$  is explained by the residual compressive stress [8]. Another important characteristic extracted from the Raman spectra is the crystallite size, which is larger than  $\sim 20 \text{ nm}$ , because the Raman peaks of the nanoparticles have almost the same half-width ( $4-5 \text{ cm}^{-1}$ ) as the peak from bulk crystalline silicon wafer ( $4.5 \text{ cm}^{-1}$ ) [5].

The Raman measurements agree with characterization of the printed nanoparticles by means of transmission electron microscopy (TEM). We used specimen grids (3-mm-diameter, 200-mesh copper grids, coated on one side with a 20-nm-thick film of amorphous carbon) to collect nanoparticles ablated from the a-Si:H film. The size, structure, and composition of the collected nanoparticles were determined using bright and dark field TEM imaging, see the inset in Fig. 8B. The analysis of the electron diffraction pattern from several nanoparticles shows clear maxima, corresponding to certain crystalline planes (Fig. 8C). Because the specimen grids were uneven, the nanoparticles were deposited at different angles to the substrate meaning that TEM imaging also provides

information on the oblateness of the particles along the direction perpendicular to the substrate surface, giving the average ellipticity about  $a_{\parallel}/a_{\perp} \approx 1.12$ , where  $a_{\parallel}(a_{\perp})$  is the particle semi-major (semi-minor) axis oriented parallel (perpendicular) to the surface of the substrate. Indeed, scanning electron microscopy (SEM, Carl Zeiss, Neon 40) confirms that the particles possess [axial](#) symmetry along the substrate normal (Fig. 8B). These results correlate with previously observed oblateness of the printed silicon nanoparticles [29].

As was reported previously [29, 19], the mean size of the printed nanoparticles strongly depends on laser fluence. In our experiments we also observed similar behavior. In particular, two different regimes of the nanoparticle generation were observed. The first regime represents the gradual growth of the nanoparticle size with an increase of fluence up to  $150 \text{ mJ/cm}^2$ , manifesting in the change of their colors from blue to red (Figs. 9A–C). Such behavior can be described in terms of the spallation mechanism of laser ablation, where a thin molten layer is spalled due to the laser-induced tensile pressure waves [61, 68], breaking into a number of liquid droplets via the Rayleigh-Plateau instability [46]. The photomechanically spalled volume increases as  $V \sim \ln(E)$  under the action of a Gaussian beam, owing to the logarithmic dependence of the spalled surface layer area  $r_s^2 \sim \ln(E)$  [2], whereas the thickness of the layer remains almost constant [61] or even decreases [68]. In previous studies of nanoparticle [generation](#) from crystalline silicon such an increase of the molten volume led to an increase in the number of nanoparticles [19] and their size [29], which agrees with our results (Fig. 9A–C).

The second regime of the nanoparticle fabrication corresponds to  $F > 150 \text{ mJ/cm}^2$ , where large (red) nanoparticles are followed by small nanoparticles with a much broader size distribution (Fig. 9D). This regime is related to unstable boiling of superheated silicon [4, 61, 68], when the nanoparticle formation occurs through explosive decomposition of the material into vapor and small clusters/droplets [27, 68], yielding nanoparticles with the mean sizes smaller than 100 nm [20]. Small silicon nanoparticles fabrication in this regime has been extensively studied over last two decades [20, 18] for a number of biomedical applications. However, one can conclude that the high-fluencies regime (Fig. 9D) is not desirable for reproducible Mie-type nanoresonators fabrication, whereas the low-fluence regimes (Fig. 9A–C) provide much more controllable nanoparticle [generation and deposition](#). The Raman, TEM and SEM characterization of the printed silicon nanoparticles helped to determine their almost perfect crystalline phase, meaning that it is possible to fabricate the crystalline silicon nanoresonators from amorphous films, which is very useful for low-loss all-dielectric nanophotonics.

### 3.2 [Characterization of Resonant Optical Modes of the Nanoparticles](#)

The excitation of the electric dipole (ED) and magnetic dipole (MD) resonances is proven by simulations in CST Microwave Studio. The scattering geometry is modeled as a c-Si ellipsoid with different axis ( $a_{\perp}$  and  $a_{\parallel}$ ) and the fixed ellipticity  $a_{\parallel}/a_{\perp} \approx 1.12$ , i.e. for the most probable ellipticity parameter in the experiments. The ellipsoid is irradiated by a plane wave at the angle  $65^\circ$

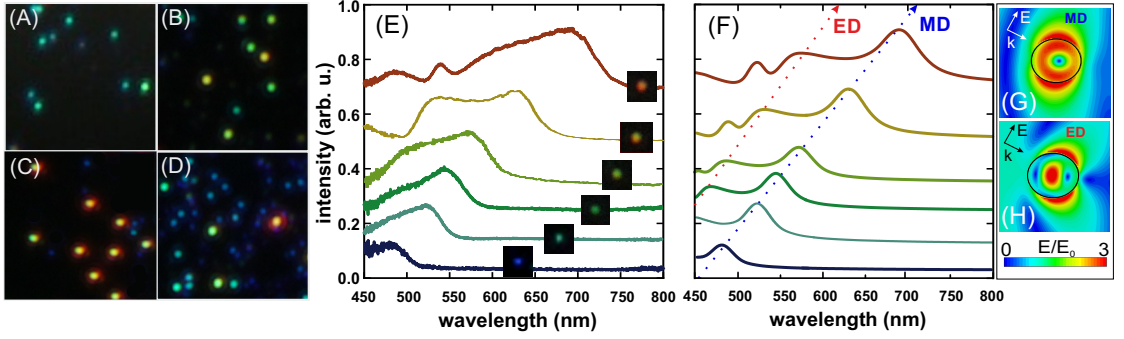


Figure 9: Dark-field optical images of silicon nanoparticles fabricated at different peak fluencies: 120 (A), 130 (B), 140 (C), 160 mJ/cm<sup>2</sup> (D). Experimental (E) and theoretical (F) spectra for scattered p-polarized incident light (angle of incidence is 65°) from individual nanoparticles with the radius parallel to substrate surface  $a_{\parallel}$  = 55 nm (blue), 65 nm (spring green), 68 nm (green), 72 nm (olive), 85 nm (yellow) and 92 nm (red) with the ellipticity coefficient of 1.12. Numerically calculated electric field distributions in the silicon nanoparticle with  $a_{\perp}$  = 85 nm the wavelengths of 635 nm (G) and 525 nm (H).

in vacuum. Modeling of scattering spectra (Fig. 9F) shows good agreement with the corresponding experimental ones (Fig. 9E), whereas the modeled electric field distributions in the ellipsoids at different wavelengths reveal excitation of MD (Fig. 9G) and ED (Fig. 9H).

### 3.3 Determining Size of Nanoparticle from Optical Resonance Positions

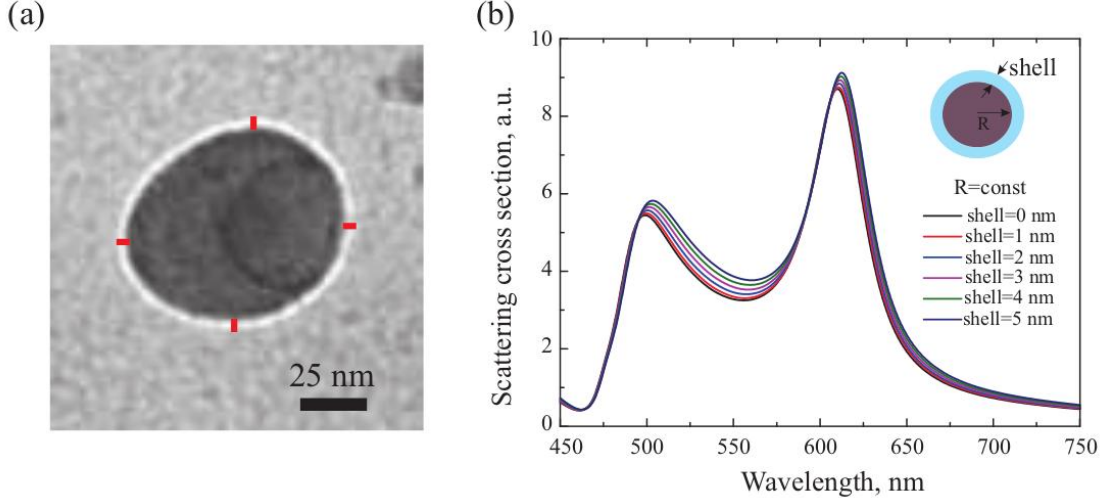


Figure 10: **a.** TEM image of the typical silicon nanoparticle fabricated using laser-induced forward transfer technique. Red lines represent 5 nm. **b.** Total scattering cross sections of silicon nanoparticle ( $R = 75$  nm) coated with silica layers with different thicknesses.

Resonant optical properties of silicon nanoparticles are known to be sensitive to their shape[[13]], crystallinity[[13, 28]], to the substrate[[57]] and to the thickness of native oxide layer[[13, 11]],

which is always present on silicon surface[[21]]. In this work, the shape of the particles has been controlled using SEM measurements, while the diameter of silicon core has been extracted from dark-field spectroscopy experiments. In order to analyze the influence of native silicon oxide layer on the optical properties of the studied nanoparticles, we carried out additional experimental measurements and numerical simulations. First, to estimate the thickness of the layer, we have characterized typical silicon nanoparticle using transmission electron microscopy (TEM), see Fig. [10A]. Our measurements confirm that nanoparticles are coated with less than 5-nm-thick silica layer, which is in good agreement with previously reported results[[13, 11]]. To analyze the influence of the oxide layer on the resonant properties of nanoparticles, we have simulated total scattering cross section spectra of a crystalline silicon nanoparticle ( $D = 150$  nm) surrounded by silica shells with different thicknesses, see Fig. [10]. For the sake of simplicity, the simulations have been carried out using Mie theory[[3]]. Our results confirm that in the case of fixed silicon core diameter appearance of additional 5-nm-thick silica layer leads to red spectral shifts of both electric and magnetic dipole resonances of the nanoparticle as small as  $\approx 4.2$  nm and  $\approx 2.5$  nm, respectively. The influence of different substrates has been analyzed in Ref. [[57]] The authors have demonstrated that both electric and magnetic dipole resonances of crystalline silicon nanoparticle placed on the fused silica substrate exhibit small red spectral shifts with respect to the resonances of the nanoparticle in free space. In the case of nanoparticle with the diameter of  $D = 130$  nm these shifts are as small as  $\approx 3.5$  nm and  $\approx 0.5$  nm, respectively. Therefore, the spectral shift of the nanoparticle's magnetic dipole resonance is practically insensitive to both the substrate and the native silica layer. This allows to conclude that the diameter of silicon core of the nanoparticle can be precisely extracted from the spectral position of magnetic dipole resonance in the dark-field spectroscopy measurements compared to the simulations based on Mie theory.

### 3.4 Raman Scattering Enhancement from Single Nanoparticles

Theoretically predicted enhancement of Raman scattering at different Mie-resonances was directly compared with our experiments with individual crystalline silicon (c-Si) nanospheres lying on a fused silica substrate (details of the fabrication are in [Methods](#)). In order to determine the resonant properties of nanoparticles, we measure their scattering spectra in the dark-field scheme (Fig. 11a, see [Methods](#) below).

In order to confirm the excitation of ED and MD resonances, we simulate numerically the scattering spectra by the method of discrete-dipole approximation (DDA) and analyze near fields by the full-wave modeling in CST Microwave Studio (for details of these calculations see [Methods](#)). The results of numerical modeling are shown in Fig. 11a, and they exhibit a good agreement with experimental results, revealing the mode structure at each spectral maximum. We use optical properties for c-Si from Ref. [59], giving the best fitting of our experimental scattering spectra. Minor differences of the results in the region of 550–600 nm may be attributed to the presence of a  $\text{SiO}_2$  substrate.

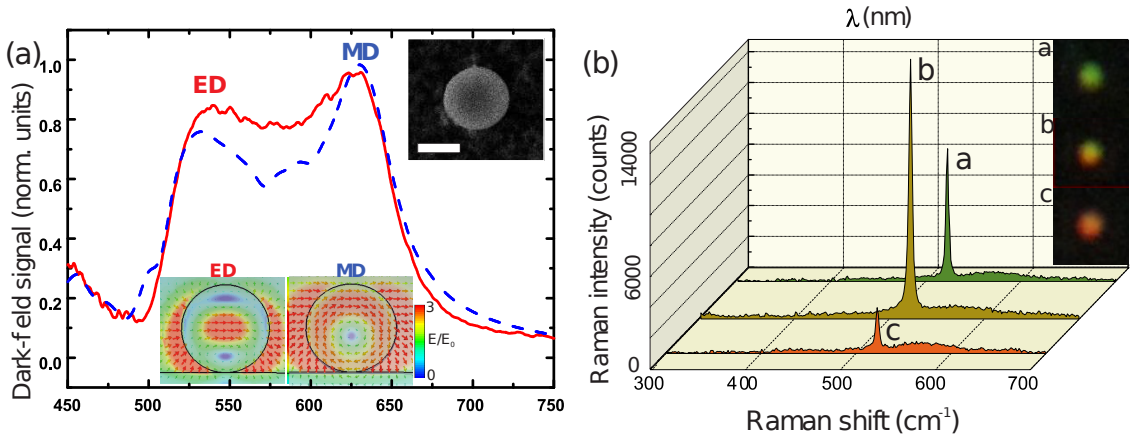


Figure 11: (a) Experimental (solid) and theoretical (dashed) scattering spectra for s-polarized incident light. Bottom inset: the electric field distribution at different wavelengths, corresponding to electric dipole (ED) and magnetic dipole (MD) resonances. Upper inset: SEM image of typical ablative c-Si nanoparticle (scale bar represents 100 nm). (b) Raman spectra for different nanoparticles at the excitation wavelength of 633 nm and the corresponding dark-field optical images of the nanoparticles: (a)  $D=153$  nm, (b)  $D=158$  nm, (c)  $D=173$  nm.

The measured Raman scattering signal from individual nanoparticles exhibits extremely strong dependence on their size and color in the dark-field images (Fig. 11b). Such a dependence for the excitation light at the wavelength  $\lambda=633$  nm shows a maximum of Raman scattering for nanoparticles with  $D \approx 155$  nm, supporting MD resonance at this wavelength. The maximum value of the enhancement factor (EF) for nanoparticles with MD in comparison with nanoparticles with diameters  $D \approx 125$  nm and  $D \approx 175$  nm is about  $EF \approx 140$ . The calculation of EF from experimental data is based on the formula:  $EF = (I/I_{\text{norm}}) \times (V/V_{\text{norm}})$ , where  $I$  is Raman scattering signal from a

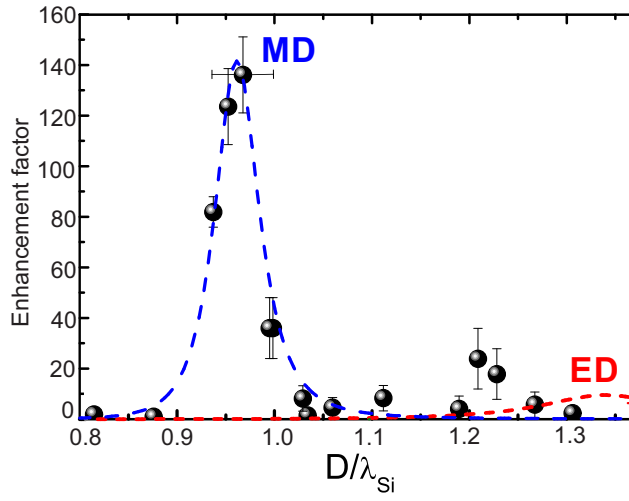


Figure 12: Theoretical (dashed curves) and experimental (black dots) dependencies of the enhancement factor for Raman scattering from spherical silicon nanoparticles on their diameter  $D$  normalized to the excitation wavelength in silicon. Theoretical dependence consists of two contributions from magnetic dipole (blue dashed curve) and electric dipole (red dashed curve).

studied nanoparticle with known diameter and volume  $V$ ,  $I_{\text{norm}}$  is Raman signal from a nanoparticle of known volume  $V_{\text{norm}}$  with the smallest observed signal. To make such a normalization, the nanoparticle with  $D \approx 135$  nm is chosen. In order to check the effect of excitation wavelength, we also measured the Raman spectra at  $\lambda=532$  nm for the same nanoparticles. Here, the maximum EF values observed for nanoparticles are relatively small at  $\lambda=633$  nm, i.e. for diameters around 125 nm and 175 nm.

In order to distinguish contributions from each type of Mie resonances, the generalized EF dependence of Raman scattering should be represented in terms of the dimensionless nanoparticle diameter  $D/\lambda_{\text{Si}}$ , taking into account different refractive indices at different wavelengths (Fig. 12). Such a dependence exhibits a pronounced maximum with a peak  $EF \approx 140$  at  $D/\lambda_{\text{Si}} \approx 1$ , i.e. near the magnetic dipole resonance. This value is 5-7 times larger than EF for the electric dipole. Insets in Fig. 11a provide an illustrative interpretation of this enhancement. At the MD resonance, a larger fraction of electromagnetic energy is stored inside the nanoparticle, thus increasing total Raman polarization and emission. Corresponding theoretical calculations for perfect spherical c-Si nanoparticles predict even larger difference between MD and ED ( $\sim 10$ ), which is not perfectly matched with our observations owing to the existence of nanoscale deviations and few-nm natural oxide layer [11, 13]. Nevertheless, the Raman signal enhancement in the vicinity of MD is in excellent agreement with our model. The data shown in Fig. 12 is limited to nanoparticle diameters  $D/\lambda_{\text{Si}} < 1.3$  as our fabrication method does not allow to make larger particles without pronounced ellipticity. At the same time, even small deviation from the spherical shape leads to suppression of the MQ resonance [11].

## Results

The main results of the project are:

1. Developed two methods for single-stage fabrication of crystalline silicon nanoparticles using femto-second laser ablation:
  - Direct laser writing of arrays of nanoparticles in an amorphous silicon thin-film
  - Forward laser transfer of crystalline nanoparticles from amorphous silicon thin-films to arbitrary substrates
2. Demonstrated crystallinity of nanoparticles by electron diffraction and Raman measurements
3. Implemented DDA modeling of apspherical nanoparticles, compared shape-dependent shifts of resonances to pure Mie-theory and FIT modeling
4. Measured elastic scattering spectra from single nanoparticles in dark-field configuration
5. Estimated sizes of nanoparticles based on positions of Mie-type resonances
6. Measured Raman scattering intensity from crystalline nanoparticles
7. Demonstrated resonant behavior of Raman signal intensity dependent on relative positions of excitation wavelength and Mie-type resonances of the nanoparticles

The results of the project were published in the peer-reviewed journal Nanoscale — “Laser fabrication of crystalline silicon nanoresonators from an amorphous film for low-loss all-dielectric nanophotonics”[28] and “Resonant Raman scattering from silicon nanoparticles enhanced by magnetic response”[54].

## **Acknowledgements**

I would like to thank D. Baranov for developing the theoretical description of the processes studied in this project.

I would like to thank V. Milichko and S. Makarov for helping with designing, optimizing and carrying the experimental work: Fabrication of nanoparticles and Raman scattering.

I would like to thank I. Mukhin for carrying out SEM experiments needed for this project.

I would like to thank A. Sitnikova for carrying out TEM and X-Ray diffractometry experiments needed for this project.

I would also like to thank my supervisors, S. Makarov and A. Samusev for their guidance during the whole duration of the project.

## A Mie Scattering of Light

An important problem for dielectric nanophotonics is the scattering of electromagnetic radiation by a homogeneous sphere. This problem has an analytical solution, generally called Mie theory[36]. The following is a condensed version of the solution, following the presentation from Ref. [42]. We will assume an x-polarized incident wave with amplitude  $E_0$ , propagation constant  $\beta_0$  traveling in the  $z$  direction:

$$\vec{E}_{inc} = E_0 e^{i\beta_0 z} \hat{x} \quad (17)$$

### A.1 Maxwell's Equations

Starting with

$$\nabla \times \vec{E} = i\omega\mu\vec{H} \quad (18)$$

$$\nabla \times \vec{H} = -i\omega\epsilon\vec{E} \quad (19)$$

Taking the rotor of the equations and substituting,

$$\nabla \times (\nabla \times \vec{E}) = i\omega\mu\nabla\vec{H} = \omega^2\epsilon\mu\vec{E} \quad (20)$$

$$\nabla \times (\nabla \times \vec{H}) = i\omega\epsilon\nabla\vec{E} = \omega^2\epsilon\mu\vec{H} \quad (21)$$

Applying the vector identity,

$$\nabla \times \nabla\vec{A} = \nabla(\nabla \cdot \vec{A}) - \nabla \cdot (\nabla\vec{A}) \quad (22)$$

We get the following wave equations

$$\nabla^2\vec{E} + k_m^2\vec{E} = 0 \quad (23)$$

$$\nabla^2\vec{H} + k_m^2\vec{H} = 0 \quad (24)$$

$$k_m^2 = \omega^2\epsilon\mu \quad (25)$$

With  $k_m$  as the wave vector in the surrounding medium. The final aim of this derivation is to get vector solutions of the wave equations. We begin by

- Transitioning to a spherical coordinate system  $r, \theta, \phi$ , since our system is spherically symmetrical
- Defining a scalar function  $\psi_{l,m}$

- Defining a constant vector  $\vec{r}$

The scalar function will be a solution of

$$\nabla^2 \psi + k_m^2 \psi = 0 \quad (26)$$

We can construct three vector solutions:

$$\vec{L} = \nabla \psi_{l,m} \quad (27)$$

$$\vec{M}_{l,m} = \nabla \times \vec{r} \psi_{l,m} \quad (28)$$

$$\vec{N}_{l,m} = \frac{1}{k_m} \nabla \times \vec{M}_{l,m} \quad (29)$$

All solutions satisfy the wave equations.  $\vec{N}_{l,m}$  and  $\vec{M}_{l,m}$  are solenoidal functions and are rotors of each other, like  $\vec{H}$  and  $\vec{E}$ .  $\vec{L}$ , on the other hand is purely longitudinal, so we omit it in this analysis.

## A.2 Scalar Solution

In spherical coordinates, the scalar solution,  $\psi_{l,m}$  of Equation 26 is a function of  $R, \theta, \phi$

$$\frac{1}{r^2} \frac{\partial}{\partial r} \left( r^2 \frac{\partial \psi}{\partial r} \right) + \frac{1}{r^2 \sin(\theta)} \frac{\partial}{\partial \theta} \left( \sin(\theta) \frac{\partial \psi}{\partial \theta} \right) + \frac{1}{r^2 \sin^2(\theta)} \frac{\partial^2 \psi}{\partial \phi^2} + k_m^2 \psi = 0 \quad (30)$$

Next, we seek a solutions that separates the variables:

$$\psi(r, \theta, \phi) = R(r)\Theta(\theta)\Phi(\phi) \quad (31)$$

Defining constants  $m, Q$ , we separate the components into separate solutions:

$$\frac{d^2 \Phi}{d\phi^2} + m^2 \Phi = 0 \quad (32)$$

$$(1 - \cos^2(\theta)) \frac{d^2 \Theta}{d(\cos(\theta))^2} - 2 \cos(\theta) \frac{d\Theta}{d(\cos(\theta))} + \left( Q - \frac{p^2}{1 - \cos^2(\theta)} \right) \Theta = 0 \quad (33)$$

$$r^2 \frac{d^2 R}{dr^2} + 2r \frac{dR}{dr} + (k_m^2 r^2 - Q^2) R = 0 \quad (34)$$

The solutions to these equations are as follows:

For  $\Phi$

$$\Phi = e^{\pm im\phi} \quad (35)$$

For  $\Theta$ , representing it as an associated Legendre equation:

$$Q = l(l+1) \rightarrow \quad (36)$$

$$\Theta = P_l^m(\nu) = \frac{(1-\nu^2)^{\frac{m}{2}}}{2^l l!} \frac{d^{l+m}(\nu^2 - 1)^l}{d(\nu)^{l+m}} \quad (37)$$

$$\nu = \cos(\theta) \quad (38)$$

From now on,  $P_l^m = P_l^m(\nu)$ .

And for  $R$

$$R = \sqrt{\frac{2}{\pi}} Z_l(p) \quad (39)$$

$$p = k_m r \quad (40)$$

Where  $Z_l(p)$  represents the radial spherical Bessel  $j_l(p)$  or first order Hankel  $h_l(p)$ .  $h_l(p)$ , being infinite in the far field are used to represent an outgoing spherical wave pattern for the scattered field.  $j_l(p)$  is finite in the origin, so it is a correct representation of incident and transmitted fields.

Combining all of these,

$$\psi_{l,m}(r, \theta, \phi) = \sqrt{\frac{1}{\pi}} Z_l(k_m r) P_l^m e^{im\phi} \quad (41)$$

or, separating into even and odd components:

$$\psi_{l,m,o}^e(r, \theta, \phi) = \sqrt{\frac{1}{\pi}} Z_l(k_m r) P_l^{m \cos(m\phi)} \quad (42)$$

### A.3 Vector Solution

Using the previous equation,

$$\vec{M}_{l,m,o}^e = \nabla \times \hat{r}(r \psi_{l,m,o}^e) \quad (43)$$

$$\vec{r} = \hat{r} r \quad (44)$$

By applying the rotor:

$$\vec{M}_{l,m}(\hat{r}) = 0 \quad (45)$$

$$\vec{M}_{l,m,o}^e = \frac{1}{r \sin(\theta)} \frac{d(r\psi)}{d\phi} \hat{\theta} - \frac{1}{r} \frac{d(r\psi)}{d\theta} \hat{\phi} \quad (46)$$

$$= \mp Z_l \frac{P_l^m}{\sin(\theta)} \cos(m\phi) \hat{\theta} - Z_l \frac{dP_l^m}{d\theta} \sin(m\phi) \hat{\phi} \quad (47)$$

And for  $\vec{N}_{m,l_o^e}$

$$\vec{N}_{l,m,o}^e = \frac{l(l+1)}{k_m r} \psi_o^e \hat{r} + \frac{1}{k_m r} \frac{d(r\vec{M}_{l,m,\phi})}{dr} \hat{\theta} + \frac{1}{k_m r} \frac{d(r\vec{M}_{l,m,\theta})}{dr} \hat{\phi} \quad (48)$$

$$= \frac{l(l+1)}{k_m r} Z_l P_l^m \cos(m\phi) \hat{r} + \frac{1}{r} \frac{d(pZ_l)}{dp} \frac{P_l^m}{d\theta} \sin(m\phi) \hat{\theta} \quad (49)$$

$$\mp m \frac{1}{p} \frac{d(pZ_l)}{dr} \frac{P_l^m}{\sin(\theta)} \sin(m\phi) \hat{\phi} \quad (50)$$

radial  $p$  needs to be replaced by  $Np$ ,  $N = \frac{N_s}{N_m}$ , which is the relative index of the sphere to the surrounding medium.

#### A.4 Incident, Scattered and Internal Fields

We assume, that an arbitrary wave, expressed by  $\vec{A}$  can be represented by a linear combination of vector functions:

$$\vec{A} = \frac{i}{\omega} \sum_{l,m} \left( A_{l,m} \vec{M}_{l,m} + B_{l,m} \vec{N}_{l,m} \right) \quad (51)$$

Since  $\vec{M}_{l,m}$  and  $\vec{N}_{l,m}$  are solenoidal function that correspond to interdependence of  $\vec{H}$  and  $\vec{E}$ , using  $\vec{A}$ :

$$\vec{H}_{inc} = \frac{1}{i\omega\mu} \nabla \times \vec{A} \quad (52)$$

$$= -\frac{i}{\omega\mu} \sum \left( A_{l,m} (\nabla \times \vec{M}_{l,m}) + B_{l,m} (\nabla \times \vec{N}_{l,m}) \right) \quad (53)$$

$$= -\frac{ik_m}{\omega\mu} \sum \left( A_{l,m} \vec{N}_{l,m} + B_{l,m} \vec{M}_{l,m} \right) \quad (54)$$

Similarly,

$$\vec{E}_{inc} = \frac{k_m}{\omega^2\epsilon\mu} \sum \left( A_{l,m} \vec{M}_{l,m} + B_{l,m} \vec{N}_{l,m} \right) \quad (55)$$

$A_{l,m}, B_{l,m}$  are expansion coefficients for a particular beam:

$$A_{l,m} = \int M_{l,m}^* \vec{E}_{inc} d\Omega \quad (56)$$

$$B_{l,m} = \int N_{l,m}^* \vec{E}_{inc} d\Omega \quad (57)$$

(58)

Where  $\Omega = 4\pi r$  is the enclosed surface area.

Similarly, the scattered and internal fields can be expanded in terms of  $\vec{M}_{l,m}, \vec{N}_{l,m}$ :

$$\vec{E}_{scat} = \frac{k_m}{\omega^2 \epsilon \mu} \sum (A_{l,m} a_l \vec{M}_{l,m} + B_{l,m} b_l \vec{N}_{l,m}) \quad (59)$$

$$\vec{H}_{scat} = -\frac{k_m}{\omega \mu} \sum (A_{l,m} a_l \vec{M}_{l,m} + B_{l,m} b_l \vec{N}_{l,m}) \quad (60)$$

$$\vec{E}_{int} = \frac{k_m}{\omega^2 \epsilon_{int} \mu} \sum (A_{l,m} c_l \vec{M}_{l,m} + B_{l,m} d_l \vec{N}_{l,m}) \quad (61)$$

$$\vec{H}_{int} = -\frac{ik_m}{\omega \mu} \sum (A_{l,m} c_l \vec{M}_{l,m} + B_{l,m} d_l \vec{N}_{l,m}) \quad (62)$$

Where  $a_l, b_l$  are scattering coefficients and  $c_d, d_l$  are internal field coefficients.

## A.5 Mie Coefficients

The Mie coefficients  $a_l, b_l, c_l, d_l$  can be determined from boundary conditions on the edge of the sphere.

$$(\vec{E}_{inc} + \vec{E}_{scat} - \vec{E}_{int}) \times \vec{r} = 0 \quad (63)$$

$$(\vec{H}_{inc} + \vec{H}_{scat} - \vec{H}_{int}) \times \vec{r} = 0 \quad (64)$$

or,

$$E_{inc,\theta} + E_{scat,\theta} = E_{int,\theta} \quad (65)$$

$$E_{inc,\phi} + E_{scat,\phi} = E_{int,\phi} \quad (66)$$

$$H_{inc,\theta} + H_{scat,\theta} = H_{int,\theta} \quad (67)$$

$$H_{inc,\phi} + H_{scat,\phi} = H_{int,\phi} \quad (68)$$

Which, substituting the vector spherical harmonics, gives:

$$j_l(N\xi)c_l + h_l(\xi)b_l = j_l(\xi) \quad (69)$$

$$[N\xi j_l(N\xi)]'c_l + [\xi h_l(\xi)]'b_l = [\xi j_l(\xi)]' \quad (70)$$

$$Nj_l(N\xi)d_l + h_l(\xi)a_l = j_l(\xi) \quad (71)$$

$$[N\xi j_l(N\xi)]'d_l + N[\xi h_l(\xi)]'a_l = N[\xi j_l(\xi)]' \quad (72)$$

which gives us the standard expressions for the Mie coefficients:

$$a_l = \frac{N^2 j_l(N\xi)[\xi j_l(\xi)]' - j_l(\xi)[N\xi j_l(N\xi)]'}{N^2 j_l(N\xi)[\xi h_l(\xi)]' - h_l(\xi)[N\xi j_l(N\xi)]'} \quad (73)$$

$$b_l = \frac{j_l(N\xi)[\xi j_l(\xi)]' - j_l(\xi)[N\xi j_l(N\xi)]'}{j_l(N\xi)[\xi h_l(\xi)]' - h_l(\xi)[N\xi j_l(N\xi)]'} \quad (74)$$

$$c_l = \frac{j_l(\xi)[\xi h_l(\xi)]' - h_l(\xi)[\xi j_l(\xi)]'}{j_l(N\xi)[\xi h_l(\xi)]' - h_l(\xi)[N\xi j_l(N\xi)]'} \quad (75)$$

$$d_l = \frac{N j_l(\xi)[\xi h_l(\xi)]' - N h_l(\xi)[\xi j_l(\xi)]'}{N^2 j_l(N\xi)[\xi h_l(\xi)]' - h_l(\xi)[N\xi j_l(N\xi)]'} \quad (76)$$

## A.6 Cross Sections

Scattering and extinction cross sections can be easily computed, knowing the Mie coefficients.

$$C_{sca} = \frac{W_{sca}}{I_{inc}} \quad (77)$$

$$C_{ext} = \frac{W_{ext}}{I_{inc}} \quad (78)$$

$$W_{sca} = \frac{1}{2} \int_0^{2\pi} \int_0^\pi (E_{sca} \times H_{sca}^*) r^2 \sin(\theta) d\theta d\phi \quad (79)$$

$$= \frac{1}{2} \int_0^{2\pi} \int_0^\pi (E_{sca,\theta} \times H_{sca,\phi}^* - E_{sca,\phi} \times H_{sca,\theta}^*) r^2 \sin(\theta) d\theta d\phi \quad (80)$$

$$W_{ext} = \frac{1}{2} \int_0^{2\pi} \int_0^\pi (E_{inc} \times H_{sca}^*) r^2 \sin(\theta) d\theta d\phi \quad (81)$$

$$= \frac{1}{2} \int_0^{2\pi} \int_0^\pi (E_{inc,\phi} \times H_{sca,\theta}^* - E_{inc,\theta} \times H_{sca,\phi}^* - E_{sca,\phi} \times H_{inc,\theta}^* + E_{sca,\theta} \times H_{inc,\phi}^*) r^2 \sin(\theta) d\theta d\phi \quad (82)$$

Which can be simplified to

$$C_{sca} = \frac{2\pi}{k_m^2} \sum_{l=1}^{\infty} (2l+1)(|a_l|^2 + |b_l|^2) \quad (83)$$

$$C_{ext} = \frac{2\pi}{k_m^2} \Re \sum_{l=1}^{\infty} (2l+1)(a_l + b_l) \quad (84)$$

$$C_{abs} = C_{ext} - C_{sca} \quad (85)$$

## B Raman Scattering from Crystalline Materials

Raman scattering of light from crystalline materials is a versatile method of probing the phonon structure of the materials. A simplistic classical model of Raman scattering is sufficient to demonstrate the effect and to properly predict many of the Raman scattering peaks of semiconductors[48].

We start with an infinite medium with electric susceptibility  $\chi$ . For simplicity, let us assume that the medium is isotropic and that the susceptibility is scalar. A plane sinusoidal wave is present in the medium, inducing sinusoidal polarization:

$$\vec{F}(\vec{r}, t) = \vec{F}_i(\vec{k}_i, \omega_i) \cos(\vec{k}_i \cdot \vec{r} - \omega_i t) \quad (86)$$

$$\vec{P}(\vec{r}, t) = \vec{P}(\vec{k}_i, \omega_i) \cos(\vec{k}_i \cdot \vec{r} - \omega_i t) \quad (87)$$

$$\vec{P}(\vec{k}_i, \omega_i) = \chi(\vec{k}_i, \omega_i) \vec{F}_i(\vec{k}_i, \omega_i) \quad (88)$$

The lattice has thermal vibrations, quantized into phonons, causing fluctuations in  $\chi$ . The atomic displacements of a phonon can also be expressed as a plane wave, with wavevector and frequency  $\vec{q}, \omega_0$ :

$$\vec{Q}(\vec{r}, t) = \vec{Q}(\vec{q}, \omega_0) \cos(\vec{q} \cdot \vec{r} - \omega_0 t) \quad (89)$$

These phonons will perturb  $\chi$ . Assuming the characteristic electronic frequencies, which determine  $\chi$  are much larger than  $\omega_0$ ,  $\chi$  can be assumed to be a function of  $\vec{Q}$ . At room temperature the amplitudes of the vibrations are small when compared to the lattice constant, meaning we can expand  $\chi$  as a Taylor series of  $\vec{Q}$ :

$$\chi(\vec{k}_i, \omega_i, \vec{Q}) = \chi_0(\vec{k}_i, \omega_i) + \frac{\partial \chi}{\partial \vec{Q}_0} \vec{Q}(\vec{r}, t) + \dots \quad (90)$$

where  $\chi_0$  is the unperturbed susceptibility and the second term is the effect of the lattice wave. Knowing this, we can express the polarization of the medium with lattice vibrations:

$$\vec{P}(\vec{r}, t, \vec{Q}) = \vec{P}_0(\vec{r}, t) + \vec{P}_{ind}(\vec{r}, t, \vec{Q}) \quad (91)$$

$$\vec{P}_0 = \chi_0(\vec{k}_i, \omega_i) \vec{F}_i(\vec{k}_i, \omega_i) \cos(\vec{k}_i \cdot \vec{r} - \omega_i t) \quad (92)$$

$$\vec{P}_{ind}(\vec{r}, t, \vec{Q}) = \frac{\partial \chi}{\partial \vec{Q}_0} \vec{Q}(\vec{r}, t) \vec{F}_i(\vec{k}_i, \omega_i) \cos(\vec{k}_i \cdot \vec{r} - \omega_i t) \quad (93)$$

Such a simplistic description only includes interaction between TO phonons and EM waves, neglecting LO phonons, which can interact with EM waves indirectly, through macroscopic EM fields, but at this moment this is not a serious deficiency.

$$\vec{P}_{ind}(\vec{r}, t, Q) = \frac{\partial \chi}{\partial \vec{Q}_0} \vec{Q}(\vec{q}, \omega_0) \cos(\vec{q} \cdot \vec{r} - \omega_0 t) \\ \times \vec{F}_i(\vec{k}_i, \omega_i) \cos(\vec{k}_i \cdot \vec{r} - \omega_i t) \quad (94)$$

$$= \frac{1}{2} \frac{\partial \chi}{\partial \vec{Q}_0} \vec{Q}(\vec{q}, \omega_0) \vec{F}_i(\vec{k}_i, \omega_i) \\ \cdot \left( \cos((\vec{q} + \vec{k}_i) \cdot \vec{r} + (\omega_0 + \omega_i)t) + \cos((\vec{q} - \vec{k}_i) \cdot \vec{r} + (\omega_0 - \omega_i)t) \right) \quad (95)$$

$\vec{P}_{ind}$  contains two sinusoidal waves - a Stokes shifted ( $\omega_S = \omega_0 - \omega_i$ ,  $\vec{k}_S = \vec{k}_i - \vec{q}$ ) and an anti-Stokes shifted wave ( $\omega_A = \omega_0 + \omega_i$ ,  $\vec{k}_A = \vec{k}_i + \vec{q}$ ). This produces Stokes and anti-Stokes scattered light, with the difference in frequency from the original wave known as the Raman shift.

Since in this case both frequency and wavevector are conserved, single-phonon raman scattering probes only zone-center phonons. Expanding the Taylor series we can easily move to multiple phonon scattering. For two phonon scattering we get combination and difference modes. If the two phonons are identical, then we observe overtone scattering. In this case there is no limit on the wavevector of the individual phonons (only that they need to be identical), meaning that overtone Raman probes the overall phonon density of states.

The intensity of the Raman scattering depends on the polarization of the incident radiation, the scattered radiation and the types of phonons participating in the scattering.

$$I_s \propto |\vec{e}_i \cdot \frac{\partial \chi}{\partial \vec{Q}} \vec{Q}(\omega_0) \cdot \vec{e}_s|^2 \quad (96)$$

This approximates  $\vec{q} = 0$  for single phonon scattering.  $\frac{\partial \chi}{\partial \vec{Q}}$  is a third-rank tensor with complex components. Introducing  $\vec{Q}_n = \vec{Q}/|\vec{Q}|$ , a unit vector in the direction of the phonon displacement, we can define a complex second rank tensor,

$$\hat{R} = \frac{\partial \chi}{\partial \vec{Q}} \vec{Q}_n \quad (97)$$

$$I_s \propto |\vec{e}_i \cdot \hat{R} \cdot \vec{e}_s|^2 \quad (98)$$

$\hat{R}$  is the Raman tensor, whose symmetry determines the symmetry of the material's Raman-active phonons. The symmetry of the Raman tensor depends on the symmetry of the medium and the active phonons.

## C Femtosecond Laser Ablation

### C.1 Generation of femtosecond laser pulses

Femtosecond laser pulse generation is usually done using chirped pulse amplification. A mode-locked seed laser is used to generate a train of low-power femtosecond pulses, which are then temporally stretched, amplified, compressed and output from the laser system. This is necessary, because the final, compressed femtosecond pulse can have extremely high peak power, which would damage the amplification system[17]. The compression and stretching is done by using dispersion to cause different wavelengths of light to travel different distances. This is usually accomplished using either two prisms and a mirror or two diffraction gratings and a mirror, though, using engineered dispersion in optical fibers is also possible[17]. Our femtosecond laser system, Femtosecond Oscillator TiF-100F by Avesta Project, is a Ti:Sapphire laser pumped by a Nd:YLF frequency doubled laser, emitting laser pulses at a central wavelength of 800 nm, with pulse duration of 100 fs, and repetition frequency of 80 MHz.

### C.2 Ultrashort-pulse laser ablation

Laser ablation by ultrashort pulses, femto- and picosecond pulses, is a very efficient technique of patterning materials, because the short pulse length minimizes the influence of heat conduction on the ablated volume — keeping the ablation very localized and controlled.

In metals and semiconductors having a large concentration of conduction band electrons, most of the light from the pulse is absorbed by conduction band electrons. The conduction band electrons thermalize within a timeframe of 10fs-1ps, while thermalization between the electrons and the lattice is much slower, on the order of 1 – 100ps, meaning that after the absorption of the laser pulse, we have a non-equilibrium state of a hot electron gas at temperature  $T_e$  and a cold lattice at  $T$ . [2]

The evolution of the temperature of the electron gas and the lattice can be described by the following heat equations:

$$C_e \frac{\partial T_e}{\partial t} = \nabla(\kappa_e \nabla T_e) - \Gamma_{e-ph}(T_e - T) + Q(x_\alpha, t) \quad (99)$$

$$C \frac{\partial T}{\partial t} = \nabla(\kappa \nabla T) + \Gamma_{e-ph}(T_e - T) \quad (100)$$

With  $C_e, C$  as the heat capacities of the electron gas and the lattice. For a 1D approximation, the source term can be written as

$$Q(z, t) = \alpha A I(t) \exp(-\alpha z) \quad (101)$$

For femtosecond pulses, heat conduction in within the lattice (first right-hand term of Eq. 100)

can be ignored. Because the heat capacity of the electron gas is much smaller than that of the lattice,  $C_e \ll C$ , the electron gas can be heated to very high transient temperatures.

$$C_e = C_0 T_e, \quad T_e \ll T_{Fermi} \equiv \frac{E_F}{k_B} \quad (102)$$

$$C_0 = \frac{\pi^2 N_e k_B}{2T_F} \quad (103)$$

$$C = const, \quad T > \theta_{Debye} \quad (104)$$

The non-equilibrium thermal conductivity of electrons can be approximated by

$$\kappa_e = \kappa_e(T) \times \frac{T_e}{T} \quad (105)$$

Where  $\kappa_e(T)$  is the normal, equilibrium, heat conductivity.

For femtosecond pulses, the characteristic cooling time of the hot electron gas due to energy exchange with the lattice is larger than the pulse duration,  $\tau_l \ll \tau_e \equiv \frac{C_e}{\Gamma_{e-ph}}$ . For  $t \ll \tau_e$  or  $\Gamma_{e-ph} T_e \ll \frac{C_e T_e}{t}$ , electron-phonon coupling can be ignored. Another reasonable approximation, considering the thermal diffusivity of electrons  $D_e = \frac{\kappa_e}{C_e}$ ,  $D_e \tau_l < \alpha^{-2}$ , is to ignore heat conduction by electrons. Then Eq. 99 simplifies to:

$$\frac{1}{2} C_0 \frac{\partial T_e^2}{\partial t} = \alpha I_a \exp(-\alpha z) \quad (106)$$

$$T_e(t) = \left( T_0^2 + \frac{2\alpha \phi_a(t)}{C_0} \exp(-\alpha z) \right)^{\frac{1}{2}} \quad (107)$$

$$\phi_a(t) = \int_0^t I_a(t') dt' \quad (108)$$

Where  $T_0$  is the initial temperature.

By the end of the pulse,  $t = \tau_l$ , we get:

$$T_e(\tau_l) \approx \left( \frac{2\alpha \phi_a}{C_0} \right)^{\frac{1}{2}} \exp \left( -2 \frac{\alpha z}{2} \right) \quad (109)$$

For times  $t \geq \tau_l$ , Equations 100 and 99, with  $Q = 0$  describe the evolution of the two systems. The electron gas then rapidly dumps all the energy to the lattice. Continuing to ignore heat conduction, the lattice temperature:

$$T \approx \frac{\alpha\phi_a}{C} \exp(-\alpha z) \quad (110)$$

$$CT = \int_0^{T_e} C_e(T'_e) dT'_e \quad (111)$$

Significant ablation will occur if  $CT \approx \Delta H_v$ , where  $\Delta H_v$  is the transition enthalpy. All of these approximations hold if  $T_e \ll \frac{E_F}{k_B}$ . The ablated depth is approximately

$$\Delta h = \frac{1}{\alpha} \ln \frac{\phi}{\phi_{th}} \quad (112)$$

$$\phi_{th} = \frac{\Delta H_v}{\alpha A} \quad (113)$$

This is a very crude approximation, that disregards energy transport by ballistic and diffusive electron propagation; lattice deformation, thermionic electron emission, etc... A more rigorous treatment would include lattice deformations caused by the heated electron gas. The deformation wave caused by the electron gas could cause the metal to fracture and ablate, without significant heating of the lattice itself.

## D Discrete Dipole Approximation

The discrete dipole approximation is a method of numerically simulating light scattering from arbitrarily shaped particles. The general idea of the method is to replace an arbitrarily shaped scatterer by a set of point dipoles and calculate the scattering by each dipole on its one plus the interaction between the dipoles. This makes calculations straightforward for scatterers of arbitrary geometries and compositions.

The following derivation is based on the derivation found in Ref. [70]. For it we assume non-magnetic materials  $\mu = 1$  and  $e^{-i\omega t}$  time dependence. For simplicity, the dielectric permittivity is assumed to be isotropic, i.e. scalar. Generalization to anisotropic scalars is generally straightforward.

The general form of the integral equation describing the electric field inside the dielectric scatterer can be written as follows:

$$\vec{E}(\vec{r}) = \vec{E}_{inc}(\vec{r}) + \int_{V \setminus V_0} d^3 r' \hat{G}(\vec{r}, \vec{r}') \chi(\vec{r}') \vec{E}(\vec{r}') \\ + \hat{M}(V_0, \vec{r}) - \hat{L}(\partial V_0, \vec{r}) \chi(\vec{r}) \vec{E}(\vec{r}) \quad (114)$$

Where  $\vec{E}_{inc}(\vec{r})$  is the incident field,  $\vec{E}(\vec{r})$  is the total field at point  $\vec{r}$ .  $\chi(\vec{r}) = \frac{\epsilon(\vec{r})-1}{4\pi}$ .  $V$  is the total volume,  $V_0 \subset V$ ,  $\vec{r} \in V_0 \setminus \partial V_0$ .

$\hat{G}(\vec{r}, \vec{r}')$  is the free space dyadic Green's function:

$$\hat{G}(\vec{r}, \vec{r}') = \left( k^2 \hat{I} + \hat{\nabla} \hat{\nabla} \right) \frac{e^{ikR}}{R} \quad (115)$$

$$= \frac{e^{ikR}}{R} \left( k^2 \left( \hat{I} - \frac{\hat{R} \hat{R}}{R^2} \right) - \frac{1 - ikR}{R^2} \left( \hat{I} - 3 \frac{\hat{R} \hat{R}}{R^2} \right) \right) \quad (116)$$

where:  $k = \frac{\omega}{c}$ ,  $\vec{R} = \vec{r} - \vec{r}'$ ,  $R = |\vec{R}|$ ,  $\hat{R} \hat{R}$  is a dyadic  $\hat{R} \hat{R}_{\mu\nu} = R_\mu R_n u$   
 $\hat{M}$  is an integral associated with the finite exclusion volume  $V_0$ :

$$\hat{M}(V_0, \vec{r}) = \int_{V_0} d^3 r' \left( \hat{G}(\vec{r}, \vec{r}') \chi(\vec{r}') \vec{E}(\vec{r}') - \hat{G}^s(\vec{r}, \vec{r}') \chi(\vec{r}') \vec{E}(\vec{r}') \right) \quad (117)$$

where  $\hat{G}^s(\vec{r}, \vec{r}')$  is the static limit ( $k \rightarrow 0$ ) of  $\hat{G}(\vec{r}, \vec{r}')$ :

$$\hat{G}^s(\vec{r}, \vec{r}') \chi(\vec{r}') \vec{E}(\vec{r}') = \hat{\nabla} \hat{\nabla} \frac{1}{R} = -\frac{1}{R^3} \left( \hat{I} - 3 \frac{\hat{R} \hat{R}}{R^2} \right) \quad (118)$$

$\hat{L}$  is the self-interaction dyadic:

$$\hat{L}(\partial V_0, vecr) = - \oint_{\partial V_0} d^2 r' \frac{\hat{n}' \hat{R}}{R^3} \quad (119)$$

Where  $\hat{n}'$  is an external normal to the surface of  $V_0$ ,  $\partial V_0$  at  $\vec{r}'$ .  $\hat{L}$  is an always real, symmetric dyadic with trace equal to  $4\pi$ .  $\hat{L}$  does not depend on the size of the volume, only on its shape.  $\hat{M}$  depends on the size of the volume and approaches 0 when the size of the volume decreases.

The original integral equation is then discretized:

$$V = \bigcup_{i=1}^N V_i \quad (120)$$

$$V_i \cap V_j = 0, i \neq j \quad (121)$$

For simplicity, the volumes are general equal, and in the DDA are called dipoles. Assuming  $\vec{r} \in V_i$  and  $V_0 = V_i$ , the first equation becomes:

$$\begin{aligned} \vec{E}(\vec{r}) &= \vec{E}_{inc}(\vec{r}) + \sum_{j \neq i} \int_{V_j} d^3 r' \hat{G}(\vec{r}, \vec{r}') \chi(\vec{r}') \vec{E}(\vec{r}') \\ &\quad + \hat{M}(V_i, \vec{r}) - \hat{L}(\partial V_i, \vec{r}) \chi(\vec{r}) \vec{E}(\vec{r}) \end{aligned} \quad (122)$$

This sum is exact. Next, we fix  $\vec{r}_i$  in each  $V_i$  — its center. Then, for  $\vec{r} = \vec{r}_i$ , we can assume that

$$\int_{V_j} d^3 r' \hat{G}(\vec{r}_i, \vec{r}') \chi(\vec{r}') \vec{E}(\vec{r}') = V_j \hat{G}_{ij} \chi(\vec{r}_j) \vec{E}(\vec{r}_j) \quad (123)$$

$$\hat{M}(V_j, \vec{r}_j) = \hat{M}_i \chi(\vec{r}_i) \vec{E}(\vec{r}_i) \quad (124)$$

meaning that the integrals depend on the values of  $\chi$ ,  $\vec{E}$  at  $\vec{r}_i$ . Further, the integral equation can be written as

$$\vec{E}_i = \vec{E}_{i,inc} + \sum_{i \neq j} \hat{G}_{ij} V_j \chi_j \vec{E}_j + (\hat{M}_i - \hat{L}_i) \chi_i \vec{E}_i \quad (125)$$

$$\vec{E}_j = \vec{E}(\vec{r}_j) \quad (126)$$

$$\vec{E}_{i,inc} = \vec{E}_{inc}(\vec{r}_j) \quad (127)$$

$$\chi_j = \chi(\vec{r}_j) \quad (128)$$

$$\hat{L}_j = \hat{L}(\partial V_j, \vec{r}_j) \quad (129)$$

Generally, the subvolumes are assumed to be small enough that

$$\vec{E}(\vec{r}) = \vec{E}_i \quad (130)$$

$$\chi(\vec{r}) = \chi_i \quad (131)$$

$$\vec{r} \in V_i \quad (132)$$

meaning that

$$\hat{M}_i^{approx} = \text{int}_{V_i} d^3 r' \left( \hat{G}(\vec{r}_i, \vec{r}') - \hat{G}^s(\vec{r}, \vec{r}') \right) \quad (133)$$

$$\hat{G}_{ij}^{approx} = \frac{1}{V_j} \int_{V_j} d^3 r' \hat{G}(\vec{r}_i, \vec{r}') \quad (134)$$

next we apply a further approximation,

$$\hat{G}_{ij}^{approx} = \hat{G}(\vec{r}_i, \vec{r}_j) \quad (135)$$

This assumption is equivalent to replacing the initial scattering volume by a set of point dipoles. It is possible to formulate the DDA with a weaker set of assumptions, but the greatly increases computational complexity.

The DDA solves for exciting electric fields:

$$\vec{E}_i^{exc} = \left( \hat{I} + \left( \hat{L}_i - \hat{M}_i \right) \chi_i \right) \vec{E}_i = \vec{E}_i - \vec{E}_i^{self} \quad (136)$$

$$\vec{E}_i^{self} = \left( \hat{M}_i - \hat{L}_i \right) \chi_i \vec{E}_i \quad (137)$$

Where  $\vec{E}_i^{self}$  is the field induced by the subvolume on itself. Then the original equation is equivalent to

$$\vec{E}_i^{inc} = \vec{E}_i^{exc} - \sum_{j \neq i} \hat{G}_{ij} \hat{\alpha}_j \vec{E}_j^{exc} \quad (138)$$

where  $\hat{\alpha}_i$  is the polarizability tensor:

$$\hat{\alpha}_i = V_i \chi_i \left( \hat{I} + \left( \hat{L}_i - \hat{M}_i \right) \chi_i \right)^{-1} \quad (139)$$

An equivalent formulation of the DDA solves for induced polarizations:

$$\vec{P}_i = \hat{\alpha}_i \vec{E}_i^{exc} = V_i \chi_i \vec{E}_i \quad (140)$$

$$\vec{E}_i^{inc} = \hat{\alpha}_i^{-1} \vec{P}_i - \sum_{j \neq i} \hat{G}_{ij} \vec{P}_j \quad (141)$$

This formulation turns out to be preferable for numerical simulations.

Different formulations of the DDA use different approximations for the polarizability tensor  $\hat{\alpha}$ . The original formulation uses the Clausius-Mossoti polarizability:

$$\hat{\alpha}_i = \hat{I} \alpha_i^{CM} = \hat{I} d^3 \frac{3}{4\pi} \frac{\epsilon_i - 1}{\epsilon_i + 2} \quad (142)$$

After determining the internal field, we can calculate the scattered fields and cross sections of the scatterer. The scattered fields obtained by taking the limit  $r \rightarrow \infty$  of the integral in the initial equation, from which all of the DDA was derived:

$$\vec{E}^{sca}(\vec{r}) = \frac{e^{ikr}}{-ikr} \vec{F}(\vec{n}) \quad (143)$$

$$\vec{F}(\vec{n}) = -ik^3 (\hat{I} - \hat{n}\hat{n}) \sum_i \int_{V_i} d^3 r' e^{-ik\vec{r}' \cdot \vec{n}} \chi(\vec{r}') \vec{E}(\vec{r}') \vec{n} = \frac{\vec{r}}{r} \quad (144)$$

Knowing  $\vec{F}(\vec{n})$ , any other necessary scattering properties can be calculated. E.g. cross sections. For an incident plane wave:

$$\vec{E}^{inc}(\vec{r}) = \vec{e}^0 e^{i\vec{k} \cdot \vec{r}} \quad (145)$$

The scattering cross section,  $C_{sca}$  is:

$$C_{sca} = \frac{1}{k^2} \oint d\Omega \left| \vec{F}(\vec{n}) \right|^2 \quad (146)$$

using internal fields, absorption and extinction cross sections:

$$C_{abs} = 4\pi k \sum_i \int_{V_i} d^3 r' \Im(\chi(\vec{r}')) \left| \vec{E}(\vec{r}') \right|^2 \quad (147)$$

$$C_{ext} = 4\pi k \sum_i \int_{V_i} d^3 r' \Im \left( \chi(\vec{r}') \vec{E}(\vec{r}') \cdot (\vec{E}^{inc}(\vec{r}'))^* \right) \quad (148)$$

$$= \frac{4\pi}{k^2} \Re \left( \vec{F} \left( \frac{\vec{k}}{k} \right) \cdot \vec{e}^{0*} \right) \quad (149)$$

These can be expressed in terms of internal fields:

$$C_{abs} = 4\pi k \sum_i V_i \Im(\chi_i) |\vec{E}_i|^2 = 4\pi k \sum_i \Im(\vec{P}_i \vec{E}_i^*) \quad (150)$$

$$C_{ext} = 4\pi k \sum_i \Im(\vec{P}_i \cdot \vec{E}_i^{inc*}) \quad (151)$$

Most errors in the DDA are related to discretization errors, shape errors or the model used to describe the polarizability tensor.

## E Finite Integration Technique

The Finite Integration Technique (FIT) is a method for discretizing the Maxwell equations onto an arbitrary grid[66]. Because the FIT deals with the integral forms of the Maxwell equations, it, Unlike the Finite-Difference Time-Domain (FDTD) methods, does not have any restrictions on the type of grid, other than that it be homeomorphic to a simplicial complex.

For the simplicity of the following derivation[51], we will assume the cells of the grid to be brick shaped. In this case the cell complex can be described as follows:

$$\Omega = [0, L_x] \times [0, L_y] \times [0, L_z] \quad (152)$$

$$\Omega_{c,x} = \{x_i, x_1, \dots, x_m\}, x_i = \frac{L_x - 0}{m} * i \quad (153)$$

$$\Omega_{c,y} = \dots \quad (154)$$

$$\Omega_{c,z} = \dots \quad (155)$$

$$\Omega_{s,x} = \{s_0, s_1, \dots, s_m - 1\}, s_i = \frac{1}{2}(x_i + x_i + 1) \quad (156)$$

$$\Omega_{s,y} = \dots \quad (157)$$

$$\Omega_{s,z} = \dots \quad (158)$$

These can be combined into 8 different three-dimensional grids, combining main ( $c$ ) and staggered ( $s$ ) grid points:

$$\Omega_{t_x, t_y, t_z} = \Omega_{t_x} \times \Omega_{t_y} \times \Omega_{t_z} \quad (159)$$

$$t_i = (c, s) \quad (160)$$

The grid is specified by cell size and overall computational domain size. Simplest case is when  $h_x = h_y = h_z$ , a uniform grid.

$$h_x = \frac{L_x}{m_x} \quad (161)$$

$$h_y = \frac{L_y}{m_y} \quad (162)$$

$$h_z = \frac{L_z}{m_z} \quad (163)$$

$$(164)$$

Discretizing of the Maxwell equations on this set of grids within the framework of the FIT is done starting with the integral form of the equations:

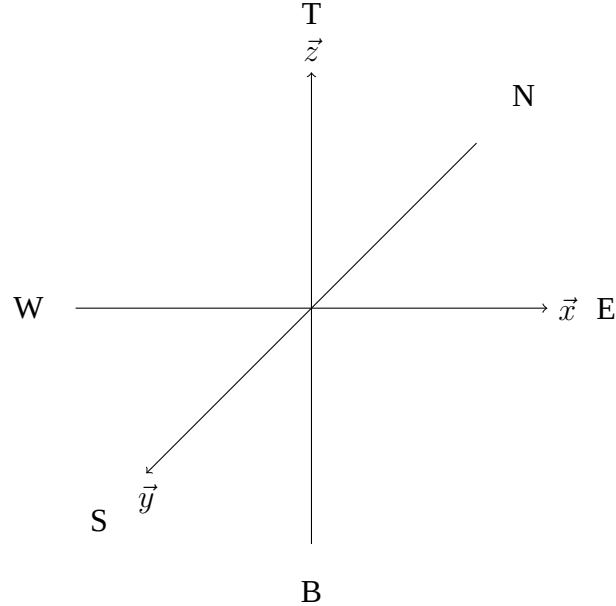


Figure 13: Schematic of used names for sides/directions of the unit cell

$$\frac{\partial}{\partial t} \int \int_{A_p} \epsilon(\vec{r}) \vec{E}(\vec{r}, t) d\vec{A} = \oint_{\partial A_p} \vec{H}(\vec{r}, t) d\vec{r} - \int \int_{A_p} \sigma(\vec{r}) \vec{E}(\vec{r}, t) d\vec{A} \quad (165)$$

$$\frac{\partial}{\partial t} \int \int_{A_p^*} \mu(\vec{r}) \vec{H}(\vec{r}, t) d\vec{A}^* = - \oint_{\partial A_p^*} \vec{E}(\vec{r}, t) d\vec{r} - \int \int_{A_p^*} \sigma^*(\vec{r}) \vec{H}(\vec{r}, t) d\vec{A}^* \quad (166)$$
  

$$(167)$$

These equations are then discretized on the staggered grid, with electric field calculated on the main grid and magnetic on the staggered one (superscript denotes timestep).

$$\frac{\vec{E}_h^{n+1} - \vec{E}_h^n}{\tau} \int \int_{A_p} \epsilon(\vec{r}) d\vec{A} = \oint_{\partial A_p} \vec{H}_h^{n+\frac{1}{2}}(\vec{r}) d\vec{r} - \vec{E}_h^{n+1} \int \int_{A_p} \sigma(\vec{r}) d\vec{A} \quad (168)$$

$$\frac{\vec{H}_h^{n+\frac{1}{2}} - \vec{H}_h^{n-\frac{1}{2}}}{\tau} \int \int_{A_p^*} \mu(\vec{r}) d\vec{A} = - \oint_{\partial A_p^*} \vec{E}_h^n(\vec{r}) d\vec{r} - \vec{H}_h^{n+\frac{1}{2}} \int \int_{A_p} \sigma^*(\vec{r}) d\vec{A}^* \quad (169)$$

Where effective permittivities and conductivities at points other than where they are defined are approximated by averaging the values from the closest available points.

for the cell depicted in Figure. 14, we have

$$d\vec{A} = \vec{n} dA = \vec{e}_x dy dz \quad (170)$$

$$d\vec{r}_y = \vec{t} dr = \vec{e}_y dy \quad (171)$$

$$d\vec{r}_z = \vec{t} dr = \vec{e}_z dz \quad (172)$$

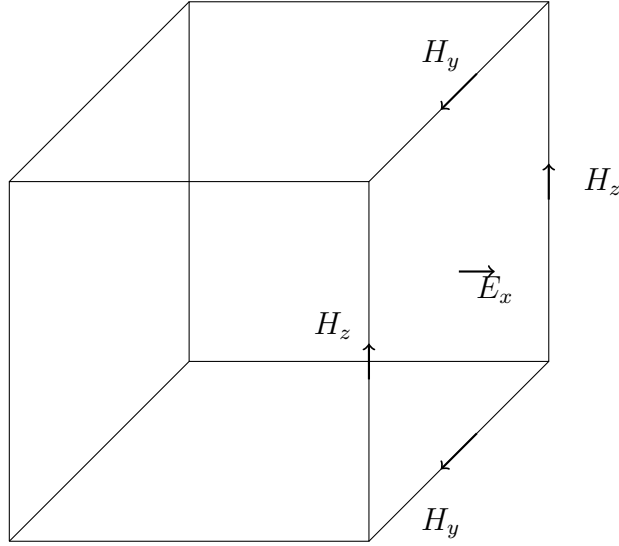


Figure 14: Surface of integration of a cell for  $E_x$  component

which means that the above equations simplify to

$$\oint_{\partial A_p} \vec{H}|_C^{n+\frac{1}{2}}(\vec{r}) d\vec{r} = \int_{C_1} H_y|_D^{n+\frac{1}{2}} - \int_{C_3} H_y|_T^{n+\frac{1}{2}} dy \quad (173)$$

$$+ \int_{C_2} H_z|_N^{n+\frac{1}{2}} dz - \int_{C_4} H_z|_S^{n+\frac{1}{2}} dz \quad (174)$$

$$= H_y|_D^{n+\frac{1}{2}} \int_{C_1} dy - H_y|_T^{n+\frac{1}{2}} \int_{C_3} dy + H_z|_N^{n+\frac{1}{2}} \int_{C_2} dz - H_z|_S^{n+\frac{1}{2}} \int_{C_4} dz \quad (175)$$

$$= H_y|_D^{n+\frac{1}{2}} \Delta y - H_y|_T^{n+\frac{1}{2}} \Delta y + H_z|_N^{n+\frac{1}{2}} \Delta z - H_z|_S^{n+\frac{1}{2}} \Delta z \quad (176)$$

$$(177)$$

Based on this, the update equations for the components of  $\vec{E}$  can be written as:

$$E_x|_M^{n+1} = \frac{1}{1 + \tau \frac{\sigma_p}{\epsilon_p}} E_x|_M^n + \frac{\frac{\tau}{\sigma_p}}{1 + \tau \frac{\sigma_p}{\epsilon_p}} \left[ \frac{H_z|_N^{n+\frac{1}{2}} - H_z|_S^{n+\frac{1}{2}}}{\Delta y} - \frac{H_y|_T^{n+\frac{1}{2}} - H_y|_D^{n+\frac{1}{2}}}{\Delta z} \right] \quad (178)$$

$$E_y|_M^{n+1} = \frac{1}{1 + \tau \frac{\sigma_p}{\epsilon_p}} E_y|_M^n + \frac{\frac{\tau}{\sigma_p}}{1 + \tau \frac{\sigma_p}{\epsilon_p}} \left[ \frac{H_x|_T^{n+\frac{1}{2}} - H_x|_D^{n+\frac{1}{2}}}{\Delta z} - \frac{H_z|_W^{n+\frac{1}{2}} - H_z|_E^{n+\frac{1}{2}}}{\Delta x} \right] \quad (179)$$

$$E_z|_M^{n+1} = \frac{1}{1 + \tau \frac{\sigma_p}{\epsilon_p}} E_z|_M^n + \frac{\frac{\tau}{\sigma_p}}{1 + \tau \frac{\sigma_p}{\epsilon_p}} \left[ \frac{H_y|_W^{n+\frac{1}{2}} - H_y|_E^{n+\frac{1}{2}}}{\Delta x} - \frac{H_x|_N^{n+\frac{1}{2}} - H_x|_S^{n+\frac{1}{2}}}{\Delta y} \right] \quad (180)$$

Using the same method, we can derive the update equations for the components of  $\text{vec}H$ :

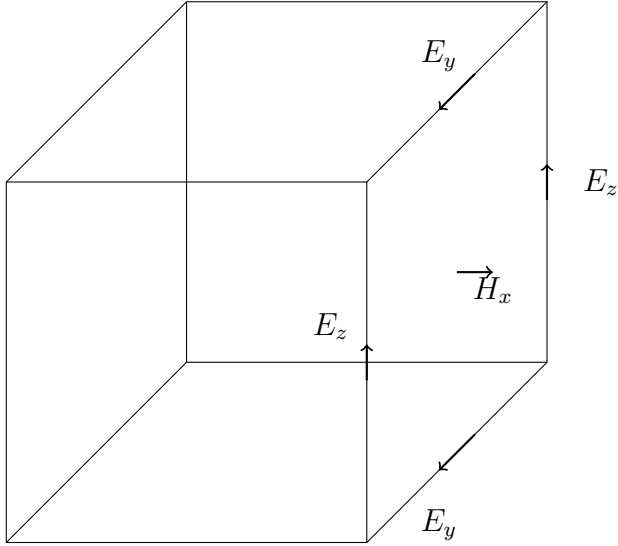


Figure 15: Surface of integration of a cell for  $H_x$  component

$$d\vec{A}^* = \vec{n}dA^* = \vec{e}_x dy dz \quad (181)$$

$$d\vec{R}_y = \vec{t}dr = \vec{e}_y dy \quad (182)$$

$$d\vec{r}_z = \vec{t}dr = \vec{e}_z dz \quad (183)$$

$$\oint_{\partial A_p} \vec{E}|_C^n(\vec{r}) d\vec{r} = \int_{C_1} E_y|_T^n dy - \int_{C_3} E_y|_D^n dy - \int_{C_2} E_z|_N^n dz + \int_{C_4} E_z|_S^n dz \quad (184)$$

$$= E_y|_T^n \int_{C_1} dy - E_y|_D^n \int_{C_3} dy - E_z|_N^n \int_{C_2} dz + E_z|_S^n \int_{C_4} dz \quad (185)$$

$$= E_y|_T^n \Delta y - E_y|_D^n \Delta y - E_z|_N^n \Delta z + E_z|_S^n \Delta z \quad (186)$$

$$H_x|_M^{n+\frac{1}{2}} = \frac{1}{1 + \tau \frac{\sigma_p^*}{\mu_p}} H_x|_M^{n-\frac{1}{2}} + \frac{\frac{\tau}{\sigma_p^*}}{1 + \tau \frac{\sigma_p^*}{\mu_p}} \left[ \frac{E_y|_T^n - E_y|_D^n}{\Delta z} - \frac{E_z|_N^n - E_z|_S^n}{\Delta y} \right] \quad (187)$$

$$H_y|_M^{n+\frac{1}{2}} = \frac{1}{1 + \tau \frac{\sigma_p^*}{\mu_p}} H_y|_M^{n-\frac{1}{2}} + \frac{\frac{\tau}{\sigma_p^*}}{1 + \tau \frac{\sigma_p^*}{\mu_p}} \left[ \frac{E_z|_T^n - E_z|_D^n}{\Delta x} - \frac{E_x|_N^n - E_x|_S^n}{\Delta z} \right] \quad (188)$$

$$H_z|_M^{n+\frac{1}{2}} = \frac{1}{1 + \tau \frac{\sigma_p^*}{\mu_p}} H_z|_M^{n-\frac{1}{2}} + \frac{\frac{\tau}{\sigma_p^*}}{1 + \tau \frac{\sigma_p^*}{\mu_p}} \left[ \frac{E_x|_T^n - E_x|_D^n}{\Delta y} - \frac{E_y|_N^n - E_y|_S^n}{\Delta x} \right] \quad (189)$$

The main advantage of using FIT over FDTD is that it is not tied to the geometry of the grid — it is easier to optimize the geometry of the grid to the geometry that is being studied.

## References

- [1] All-dielectric optical nanoantennas / Alexander E Krasnok, Andrey E Miroshnichenko, Pavel A Belov, Yuri S Kivshar // Optics Express. — 2012. — Vol. 20, no. 18. — P. 20599–20604.
- [2] Bäuerle Dieter W. Laser processing and chemistry. — Springer Science & Business Media, 2013.
- [3] Bohren Craig F, Huffman Donald R. Absorption and scattering by a sphere // Absorption and Scattering of Light by Small Particles. — 1983. — P. 82–129.
- [4] Bulgakova NM, Bulgakov AV. Pulsed laser ablation of solids: transition from normal vaporization to phase explosion // Applied Physics A: Materials Science & Processing. — 2001. — Vol. 73, no. 2. — P. 199–208.
- [5] Campbell IH, Fauchet Ph M. The effects of microcrystal size and shape on the one phonon Raman spectra of crystalline semiconductors // Solid State Communications. — 1986. — Vol. 58, no. 10. — P. 739–741.
- [6] Controllable femtosecond laser-induced dewetting for plasmonic applications / Sergey V Makarov, Valentin A Milichko, Ivan S Mukhin et al. // Laser & Photonics Reviews. — 2016. — Vol. 10, no. 1. — P. 91–99.
- [7] Courant Richard. Variational methods for the solution of problems of equilibrium and vibrations // Lecture Notes in Pure and Applied Mathematics. — 1994. — P. 1–1.
- [8] De Wolf Ingrid. Micro-Raman spectroscopy to study local mechanical stress in silicon integrated circuits // Semiconductor Science and Technology. — 1996. — Vol. 11, no. 2. — P. 139.
- [9] Deterministic measurement of the Purcell factor in microcavities through Raman emission / X Checoury, Z Han, M El Kurdi, P Boucaud // Physical Review A. — 2010. — Vol. 81, no. 3. — P. 033832.
- [10] Direct Femtosecond Laser Writing of Optical Nanoresonators / PA Dmitriev, SV Makarov, VA Milichko et al. // Journal of Physics: Conference Series / IOP Publishing. — Vol. 690. — 2016. — P. 012021.
- [11] Directional visible light scattering by silicon nanoparticles / Yuan Hsing Fu, Arseniy I Kuznetsov, Andrey E Miroshnichenko et al. // Physical Review Letters. — 2012.
- [12] Effect of perturbations on the widths of narrow morphology-dependent resonances in Mie scattering / HM Lai, CC Lam, Peter T Leung, Kenneth Young // JOSA B. — 1991. — Vol. 8, no. 9. — P. 1962–1973.

- [13] Electromagnetic resonances of silicon nanoparticle dimers in the visible / Urs Zywietz, Mikolaj K Schmidt, Andrey B Evlyukhin et al. // ACS Photonics. — 2015. — Vol. 2, no. 7. — P. 913–920.
- [14] Enhanced third-harmonic generation in silicon nanoparticles driven by magnetic response / Maxim R Shcherbakov, Dragomir N Neshev, Ben Hopkins et al. // Nano letters. — 2014. — Vol. 14, no. 11. — P. 6488–6492.
- [15] Experimental demonstration of a broadband all-dielectric metamaterial perfect reflector / Parikshit Moitra, Brian A Slovick, Zhi Gang Yu et al. // Applied Physics Letters. — 2014. — Vol. 104, no. 17. — P. 171102.
- [16] Experimental demonstration of superdirective dielectric antenna / Alexander E Krasnok, Dmitry S Filonov, Constantin R Simovski et al. // Applied Physics Letters. — 2014. — Vol. 104, no. 13. — P. 133502.
- [17] Femtosecond laser ablation: Fundamentals and applications / Sivanandan S Harilal, Justin R Freeman, Prasoon K Diwakar, Ahmed Hassanein // Laser-Induced Breakdown Spectroscopy. — Springer, 2014. — P. 143–166.
- [18] Formation of silicon nanoparticles and web-like aggregates by femtosecond laser ablation in a background gas / BR Tull, JE Carey, MA Sheehy et al. // Applied Physics A: Materials Science & Processing. — 2006. — Vol. 83, no. 3. — P. 341–346.
- [19] Generation and patterning of Si nanoparticles by femtosecond laser pulses / Urs Zywietz, Carsten Reinhardt, Andrey B Evlyukhin et al. // Applied Physics A. — 2014. — Vol. 114, no. 1. — P. 45–50.
- [20] Generation of silicon nanoparticles via femtosecond laser ablation in vacuum / S Amoruso, R Bruzzese, N Spinelli et al. // Applied Physics Letters. — 2004. — Vol. 84, no. 22. — P. 4502–4504.
- [21] Growth of native oxide on a silicon surface / M Morita, T Ohmi, E Hasegawa et al. // Journal of Applied Physics. — 1990. — Vol. 68, no. 3. — P. 1272–1281.
- [22] Hayes William, Loudon Rodney. Scattering of light by crystals. — Courier Corporation, 2012.
- [23] High-efficiency dielectric Huygens' surfaces / Manuel Decker, Isabelle Staude, Matthias Falkner et al. // Advanced Optical Materials. — 2015. — Vol. 3, no. 6. — P. 813–820.
- [24] High-transmission dielectric metasurface with  $2\pi$  phase control at visible wavelengths / Ye Feng Yu, Alexander Y Zhu, Ramón Paniagua-Domínguez et al. // Laser & Photonics Reviews. — 2015. — Vol. 9, no. 4. — P. 412–418.

- [25] Ishimaru Akira. Electromagnetic wave propagation, radiation, and scattering. — Prentice-Hall, 1991.
- [26] Islam Mohammed N, De Wilde Carl, Kuditcher Amos. Wideband raman amplifiers // Raman Amplifiers for Telecommunications 2. — Springer, 2004. — P. 445–490.
- [27] Itina Tatiana E. Molecular dynamics study of the role of material properties on nanoparticles formed by rapid expansion of a heated target // Applied Surface Science. — 2009. — Vol. 255, no. 10. — P. 5107–5111.
- [28] Laser fabrication of crystalline silicon nanoresonators from an amorphous film for low-loss all-dielectric nanophotonics / PA Dmitriev, SV Makarov, VA Milichko et al. // Nanoscale. — 2016. — Vol. 8, no. 9. — P. 5043–5048.
- [29] Laser printing of silicon nanoparticles with resonant optical electric and magnetic responses / Urs Zywietz, Andrey B Evlyukhin, Carsten Reinhardt, Boris N Chichkov // Nature communications. — 2014. — Vol. 5.
- [30] Li HH. Refractive index of silicon and germanium and its wavelength and temperature derivatives // Journal of Physical and Chemical Reference Data. — 1980. — Vol. 9, no. 3. — P. 561–658.
- [31] Liu JM. Simple technique for measurements of pulsed Gaussian-beam spot sizes // Optics letters. — 1982. — Vol. 7, no. 5. — P. 196–198.
- [32] Loke Vincent LY, Mengüç M Pinar, Nieminen Timo A. Discrete-dipole approximation with surface interaction: Computational toolbox for MATLAB // Journal of Quantitative Spectroscopy and Radiative Transfer. — 2011. — Vol. 112, no. 11. — P. 1711–1725.
- [33] Low-loss electric and magnetic field-enhanced spectroscopy with subwavelength silicon dimers / Pablo Albella, M Ameen Poyli, Mikolaj K Schmidt et al. // The Journal of Physical Chemistry C. — 2013. — Vol. 117, no. 26. — P. 13573–13584.
- [34] Magnetic and electric hotspots with silicon nanodimers / Reuben M Bakker, Dmitry Permyakov, Ye Feng Yu et al. // Nano Letters. — 2015. — Vol. 15, no. 3. — P. 2137–2142.
- [35] Magnetic light / Arseniy I Kuznetsov, Andrey E Miroshnichenko, Yuan Hsing Fu et al. // Scientific reports. — 2012. — Vol. 2.
- [36] Mie Gustav. Beiträge zur Optik trüber Medien, speziell kolloidaler Metallösungen // Annalen der physik. — 1908. — Vol. 330, no. 3. — P. 377–445.
- [37] Mie resonance-based dielectric metamaterials / Qian Zhao, Ji Zhou, Fuli Zhang, Didier Lippons // Materials Today. — 2009. — Vol. 12, no. 12. — P. 60–69.

- [38] Monodisperse silicon nanocavities and photonic crystals with magnetic response in the optical region / Lei Shi, Justin T Harris, Roberto Fenollosa et al. // Nature communications. — 2013. — Vol. 4. — P. 1904.
- [39] Moskovits Martin. Surface-enhanced spectroscopy // Reviews of modern physics. — 1985. — Vol. 57, no. 3. — P. 783.
- [40] Murphy DV, Brueck SRJ. Enhanced Raman scattering from silicon microstructures // Optics letters. — 1983. — Vol. 8, no. 9. — P. 494–496.
- [41] A New Dielectric Metamaterial Building Block with a Strong Magnetic Response in the Sub-1.5-Micrometer Region: Silicon Colloid Nanocavities / Lei Shi, T Umut Tuzer, Roberto Fenollosa, Francisco Meseguer // Advanced materials. — 2012. — Vol. 24, no. 44. — P. 5934–5938.
- [42] Ng Li Na. Manipulation of particles on optical waveguides : Ph. D. thesis / Li Na Ng ; University of Southampton, Faculty of Engineering and Applied Science. — 2000.
- [43] Non-plasmonic nanoantennas for surface enhanced spectroscopies with ultra-low heat conversion / Martín Caldarola, Pablo Albella, Emiliano Cortés et al. // Nature communications. — 2015. — Vol. 6.
- [44] Optical response features of Si-nanoparticle arrays / Andrey B Evlyukhin, Carsten Reinhardt, Andreas Seidel et al. // Physical Review B. — 2010. — Vol. 82, no. 4. — P. 045404.
- [45] Palik Edward D. Handbook of optical constants of solids. — Academic press, 1998. — Vol. 3.
- [46] Papageorgiou Demetrios T. On the breakup of viscous liquid threads // Physics of Fluids. — 1995. — Vol. 7, no. 7. — P. 1529–1544.
- [47] Pask H Ml. The design and operation of solid-state Raman lasers // Progress in Quantum Electronics. — 2003. — Vol. 27, no. 1. — P. 3–56.
- [48] Peter YU, Cardona Manuel. Fundamentals of semiconductors: physics and materials properties. — Springer Science & Business Media, 2010.
- [49] Popa Bogdan-Ioan, Cummer Steven A. Compact dielectric particles as a building block for low-loss magnetic metamaterials // Physical review letters. — 2008. — Vol. 100, no. 20. — P. 207401.
- [50] Probing magnetic and electric optical responses of silicon nanoparticles / Dmitry Permyakov, Ivan Sinev, Dmitry Markovich et al. // Applied Physics Letters. — 2015. — Vol. 106, no. 17. — P. 171110.

- [51] Rahimi Zhabiz. The Finite Integration Technique (FIT) and the Application in Lithography Simulations : Ph. D. thesis / Zhabiz Rahimi ; Technischen Fakultät der Universität Erlangen-Nürnberg. — 2011.
- [52] Ralston JM, Chang RK. Spontaneous-Raman-scattering efficiency and stimulated scattering in silicon // Physical Review B. — 1970. — Vol. 2, no. 6. — P. 1858.
- [53] Realizing optical magnetism from dielectric metamaterials / James C Ginn, Igal Brener, David W Peters et al. // Physical review letters. — 2012. — Vol. 108, no. 9. — P. 097402.
- [54] Resonant Raman scattering from silicon nanoparticles enhanced by magnetic response / Pavel A Dmitriev, Denis G Baranov, Valentin A Milichko et al. // Nanoscale. — 2016. — Vol. 8, no. 18. — P. 9721–9726.
- [55] Spinelli P, Verschuuren MA, Polman A. Broadband omnidirectional antireflection coating based on subwavelength surface Mie resonators // Nature communications. — 2012. — Vol. 3. — P. 692.
- [56] Strong magnetic response of submicron silicon particles in the infrared / Aitzol García-Etxarri, R Gómez-Medina, Luis S Froufe-Pérez et al. // Optics express. — 2011. — Vol. 19, no. 6. — P. 4815–4826.
- [57] Substrate-induced resonant magnetoelectric effects for dielectric nanoparticles / Andrey E Miroshnichenko, Andrey B Evlyukhin, Yuri S Kivshar, Boris N Chichkov // ACS Photonics. — 2015. — Vol. 2, no. 10. — P. 1423–1428.
- [58] Superdirective dielectric nanoantennas / Alexander E Krasnok, Constantin R Simovski, Pavel A Belov, Yuri S Kivshar // Nanoscale. — 2014. — Vol. 6, no. 13. — P. 7354–7361.
- [59] Temperature dependence of the dielectric function of silicon using in situ spectroscopic ellipsometry / G Vuye, S Fisson, V Nguyen Van et al. // Thin Solid Films. — 1993. — Vol. 233, no. 1-2. — P. 166–170.
- [60] Theory of spatial coherence in near-field Raman scattering / Luiz Gustavo Cançado, Ryan Beams, Ado Jorio, Lukas Novotny // Physical Review X. — 2014. — Vol. 4, no. 3. — P. 031054.
- [61] Thermal melting and ablation of silicon by femtosecond laser radiation / AA Ionin, SI Kudryashov, LV Seleznev et al. // Journal of Experimental and Theoretical Physics. — 2013. — Vol. 116, no. 3. — P. 347–362.
- [62] Thompson Carl V. Solid-state dewetting of thin films // Annual Review of Materials Research. — 2012. — Vol. 42. — P. 399–434.

- [63] Towards all-dielectric metamaterials and nanophotonics / Alexander Krasnok, Sergey Makarov, Mikhail Petrov et al. // SPIE Optics+ Optoelectronics / International Society for Optics and Photonics. — 2015. — P. 950203–950203.
- [64] Tuning of magnetic optical response in a dielectric nanoparticle by ultrafast photoexcitation of dense electron–hole plasma / Sergey Makarov, Sergey Kudryashov, Ivan Mukhin et al. // Nano letters. — 2015. — Vol. 15, no. 9. — P. 6187–6192.
- [65] Wafer scale formation of monocrystalline silicon-based mie resonators via silicon-on-insulator dewetting / Marco Abbarchi, Meher Naffouti, Benjamin Vial et al. // ACS nano. — 2014. — Vol. 8, no. 11. — P. 11181–11190.
- [66] Weiland M Clemens T. Discrete electromagnetism with the finite integration technique // Progress In Electromagnetics Research. — 2001. — Vol. 32. — P. 65–87.
- [67] Wieland T. A discretization method for the solution of Maxwell's equations for six-components fields // Electronics and Communications AEU. — 1977. — Vol. 31, no. 3. — P. 116–120.
- [68] Wu Chengping, Zhigilei Leonid V. Microscopic mechanisms of laser spallation and ablation of metal targets from large-scale molecular dynamics simulations // Applied Physics A. — 2014. — Vol. 114, no. 1. — P. 11–32.
- [69] Yee Kane. Numerical solution of initial boundary value problems involving Maxwell's equations in isotropic media // IEEE Transactions on antennas and propagation. — 1966. — Vol. 14, no. 3. — P. 302–307.
- [70] Yurkin Maxim A, Hoekstra Alfons G. The discrete dipole approximation: an overview and recent developments // Journal of Quantitative Spectroscopy and Radiative Transfer. — 2007. — Vol. 106, no. 1. — P. 558–589.
- [71] Zambrana-Puyalto Xavier, Bonod Nicolas. Purcell factor of spherical Mie resonators // Physical Review B. — 2015. — Vol. 91, no. 19. — P. 195422.